

Air-Entrainment Mechanisms in Plunging Jets and Breaking Waves

Kenneth T. Kiger and James H. Duncan

Department of Mechanical Engineering, University of Maryland, College Park, Maryland 20742; email: kkiger@eng.umd.edu, duncan@umd.edu

Annu. Rev. Fluid Mech. 2012. 44:563–96

First published online as a Review in Advance on October 27, 2011

The *Annual Review of Fluid Mechanics* is online at fluid.annualreviews.org

This article's doi:
10.1146/annurev-fluid-122109-160724

Copyright © 2012 by Annual Reviews.
All rights reserved

0066-4189/12/0115-0563\$20.00

Keywords

aeration, drop impact, plunging breaker, air-sea interaction

Abstract

Air entrainment in liquids is a complex phenomenon that has important applications in industry and the environment. This article addresses recent research on how air is entrained during the impact of a liquid stream on a pool of the same material in a variety of scenarios. At the fundamental level, these scenarios include the prototype flows of impacting stationary laminar and turbulent steady jets, the transient impact of isolated masses of liquid, the impact of jets with organized disturbances, and translating steady and transient jets. Although significant advances have been made recently, the complexity of this multiphase, three-dimensional, and frequently turbulent flow phenomenon leaves many unanswered questions. To help elucidate the problems still to be addressed in future research, the final section of the article examines air entrainment in the more complex application of plunging breaking waves and points out the many parts of this process that are poorly understood.

1. INTRODUCTION AND SCOPE

Air entrainment in liquids is a ubiquitous phenomenon in many natural and engineering applications. It is responsible for the bulk of mass transfer that occurs at the free surface of oceans, rivers, and streams, providing the transport of oxygen and carbon dioxide (which are critical to the survival of these ecosystems), as well as playing a central role in the global climate evolution. Air entrainment is also important in naval hydrodynamics because of the breakup of the entrained air into numerous bubbles, which provide a source of acoustic noise, surfactant scavenging, and cavitation nuclei in the boundary layer and wake of ships, modifying their hydrodynamic performance and visibility to detection. In hydraulic engineering, controlled aeration is often used to protect large spillways from cavitation damage, whereas in industrial processes, aeration can be either beneficial, as in the cases in which it is used to promote maximal contact in gas-liquid reactors, or detrimental, such as in the casting of polymers or glass.

In this review, we focus on highlighting the role of air-entrainment mechanisms within two types of flows: (a) a simple prototype flow described by a plunging fluid stream moving into a receiving pool of the same liquid and (b) the more applied problem of a plunging breaking wave. The first type is a class of flows that has been widely studied for its simplicity as a prototype in other systems and as an application in and of itself for engineering purposes. The second flow is a more complex problem, but features of this flow have been modeled as a plunging jet. Hence we attempt to draw the mechanistic connections between these two flows and point out where such connections have been successful or not.

With this objective in mind, we do not review the full range of closely related aerating flows, such as the ballistic impact of rigid bodies (Duclaux et al. 2007, Korobkin & Pukhnachov 1988, May 1952) and self-aeration due to turbulent flow in channels (Chanson 1997, Wood 1991). Although quite important to most applications, we also do not discuss the fate of the gas once it has been entrained (e.g., how it breaks up into smaller bubbles, is dispersed, and eventually rises to the surface or is absorbed) and instead focus on mechanisms and models for gas entrainment. Finally, we omit many details contained in prior reviews, except in cases in which they are directly relevant for explanation of more recent advances. Some key reviews on the topic can be found in Bin (1993) and Chanson (1996), both of which emphasize subsurface breakup and dispersion.

2. PROTOTYPE FLOW: THE PLUNGING JET

The prototype flow of a plunging jet consists of an oncoming fluid stream of velocity U_j contacting a receiving pool of the same liquid. The oncoming stream is oriented with respect to the gas/liquid interface tangent vector with an angle θ_j . In most applications, the receiving pool is in a stationary reference frame and is large in comparison with the oncoming stream. There are, however, some flows in which it may be moving (e.g., in a plunging breaking wave) or constitutes a limited region supported over the oncoming stream (e.g., in a hydraulic jump or the toe region of a breaking wave). In the discussion that follows, we typically reference the local conditions of the jet at the point of contact between the jet and the pool, denoted with a subscript j and, where needed, indicate upstream jet conditions with a subscript o .

2.1. Dimensional Parameters

The quantities of interest for air entrainment are the minimum critical velocity for entrainment, U_c , and the resulting volumetric flow rate of air being entrained once the threshold is exceeded, Q_a . Because the minimum critical entrainment velocity is a specific value of the independent

variable U_j , we retain only the impact velocity in the general analysis. Simplifying the geometry of the general problem to a single reference length L for the time being, these dependent variables for the problem are functions of the fluid properties and the local conditions near the contacting point:

$$Q_a = f(L, U_j, g, \rho_\ell, \rho_g, \mu_\ell, \mu_g, \sigma, u', \lambda, \theta_j), \quad (1)$$

where g is the acceleration constant due to gravity, ρ is the density, μ is the dynamic viscosity, σ is the interfacial tension, u' is the fluctuation velocity of the local disturbances, and λ is the wavelength of the disturbances. The subscripts ℓ and g refer to properties of the liquid and gas, respectively. There are numerous nondimensionalizations for this problem, but one of the more useful ones results in

$$\frac{Q_a}{Q_\ell} = \hat{f}\left(\text{Fr}, \text{We}, \text{Ca}, \frac{\rho_g}{\rho_\ell}, \frac{\mu_g}{\mu_\ell}, \frac{u'}{U_j}, \frac{\lambda}{L}, \theta_j\right), \quad (2)$$

where the above nondimensional variables are defined in the sidebar, Nondimensional Groups Relevant to Air Entrainment. We also note that using other combinations, one can also arrive at several alternative groups: the Reynolds number, Re ; the Ohnesorge number, Oh ; and the Bond number, Bo (see definitions in the sidebar).

The use of Re is typically only helpful in distinguishing between laminar and turbulent conditions, and in specific cases in which the oncoming stream is generated by a nozzle it has been used to correlate to the disturbance state of the oncoming flow in place of u'/U_j and λ/L . The Ohnesorge

NONDIMENSIONAL GROUPS RELEVANT TO AIR ENTRAINMENT

Starting with the dimensional variables listed in Equation 1, the most common nondimensional forms found in the literature are presented under the Primary groups heading. Less frequently, alternative groupings are used, as shown in the list under Alternate groups. The impact angle, θ , is already dimensionless and that the ratio of length scales, λ , does not have its own named variable.

Primary groups:

$$\text{Froude number, Fr} = \frac{U_j^2}{gL}$$

$$\text{Weber number, We} = \frac{\rho_\ell U_j^2 L}{\sigma}$$

$$\text{capillary number, Ca} = \frac{\mu_\ell U_j}{\sigma}$$

$$\text{density ratio, } \gamma = \frac{\rho_g}{\rho_\ell}$$

$$\text{viscosity ratio, M} = \frac{\mu_g}{\mu_\ell}$$

$$\text{fluctuation intensity, } U^* = \frac{u'}{U_j}$$

Alternate groups:

$$\text{Reynolds number, Re} = \frac{\text{We}}{\text{Ca}} = \frac{\rho_\ell U_j L}{\mu_\ell}$$

$$\text{Ohnesorge number, Oh} = \frac{\text{Ca}}{\sqrt{\text{We}}} = \sqrt{\frac{\text{Ca}}{\text{Re}}} = \frac{\mu_\ell}{\sqrt{\rho_\ell \sigma L}}$$

$$\text{Bond number, Bo} = \frac{\text{We}}{\text{Fr}} = \frac{\rho_\ell \ell g L^2}{\sigma}$$

and Bond number are used much less frequently, with the Ohnesorge number appearing when correlating turbulent viscous jets (Bin 1993, El Hammoumi et al. 2002) and the Bond number appearing when describing the static meniscus away from the entrainment location (Lorenceanu et al. 2003).

2.2. Entrainment Inception Conditions

A key aspect to air entrainment is delimiting the conditions under which it occurs. That such a condition should exist can be seen from a simple energetics argument, in that a minimum amount of energy needs to be available in the flow to entrap the air—to do work against surface tension and/or the potential energy due to gravity. From the possible dimensional quantities outlined above, it has been found empirically that the impact velocity of the liquid (U_j) plays a dominant role, so much so that the entrainment criteria are often reported as critical entrainment velocities. The remainder of the current section reviews the evolution of the flow leading up to entrainment, followed in Sections 2.3 and 2.4 by a discussion of the mechanisms associated with the entrainment conditions and the air-entrainment rate once these critical conditions are exceeded for the different regimes associated with plunging jets.

Below the threshold conditions required for air entrainment, the free surface is observed to assume a shape that provides a steady or quasi-steady force balance between the subsurface flow and the surrounding free surface (**Figure 1**). For laminar jets, the meniscus is steady and may either predominantly rise up to meet the plunging liquid (**Figure 2g**) or form a concave down depression (**Figure 2a**), depending on the relative stress magnitude at the plunging contact point in comparison with that generated by interfacial tension (**Figure 1a**). For high-viscosity liquids, the stress is imposed by the viscous shear (Bin 1993, Lorenceanu et al. 2004), whereas for low-viscosity liquids, it is thought to result from the low pressure from the entrainment of fluid into the submerged jet or air entrained in a boundary layer surrounding the jet before impact (Bin 1993, Sene 1988). As the impact velocity of the liquid stream is increased, the local stress at the boundary is increased, and the meniscus is pulled further below the free surface such that the minimum radius of curvature, r , is decreased and the balance with surface tension is maintained. The critical condition is finally reached when either (a) a steady-state solution is no longer possible owing to a singularity developing at what becomes a cusp in the meniscus (**Figures 1b** and **2a-f**) or (b) the interface is destabilized by disturbances within the impinging stream and/or receiving pool, which result in the entrapment of a gas volume below the free surface. The latter case may also be subdivided, somewhat arbitrarily, into small disturbances [such that the jet still appears smooth and laminar (**Figure 1c**)] and finite-amplitude disturbances [in which the jet appears visibly rough (**Figure 1d**)], as the entrainment mechanisms for these two cases seem to be different. The details of the entrainment process for these various conditions are discussed below.

2.3. Entrainment by Viscous Plunging Jets

Lin & Donnelly (1966) were one of the first to quantitatively study the inception conditions for highly viscous fluids over a fairly broad range of viscosity. In addition to examining the influence of the liquid viscosity, they documented the effect of the jet diameter, velocity profile, surfactants, and external gas properties and proposed a correlation for the critical entrainment condition of the form

$$\text{We}_c = 10\text{Re}_c^{0.74}, \quad (3)$$

where the length scale was taken to be the diameter of the jet at impact, $L = D_j$. The correlation was found to be accurate over two orders of magnitude (all data within approximately $\pm 20\%$).

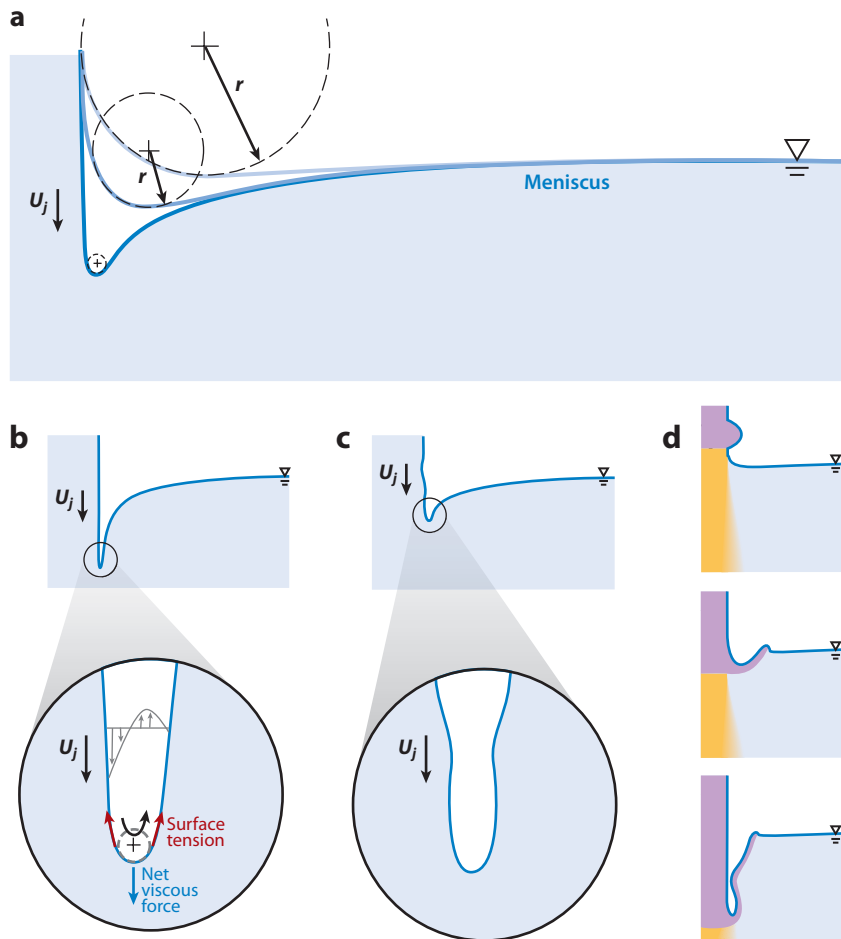


Figure 1

Schematic of a region close to the plunging impact for entrainment-inception conditions: (a) evolution of the meniscus with increasing impact velocity, U_j (the minimum radius of curvature of the meniscus, r , is indicated by the dashed circle), (b) incipient conditions for shear-dominated viscous entrainment, (c) incipient conditions for a low-viscosity, low-disturbance level, and (d) entrainment by large-amplitude disturbances. Panel *d* adapted from van de Sande (1974) and Zhu et al. (2000).

This corresponded to a range of Reynolds numbers up to 1,500, beyond which instabilities in the jet altered the nature of the entrainment mechanism to that of a laminar disturbed flow condition. This correlation has stood as the de facto relationship for viscous liquids since it was proposed, despite the lack of a physical argument as to why it should take that particular form.

Recent work concerning fluid entrainment at a viscous interface, however, has provided new insight into the physical explanation behind the inception mechanism and its scaling, at least for the case of small inertia (Eggers 2001; Lorenceau et al. 2003, 2004). The mechanism is based on the sudden formation of a singular cusp at the jet/pool intersection as the inception condition is approached. The onset of air entrainment subsequently results from a visco-capillary mechanisms that destroys the steady cusp solution via viscous pumping of the entrained fluid within the narrowing gap. These ideas were based on early experimental work by Joseph et al. (1991), who

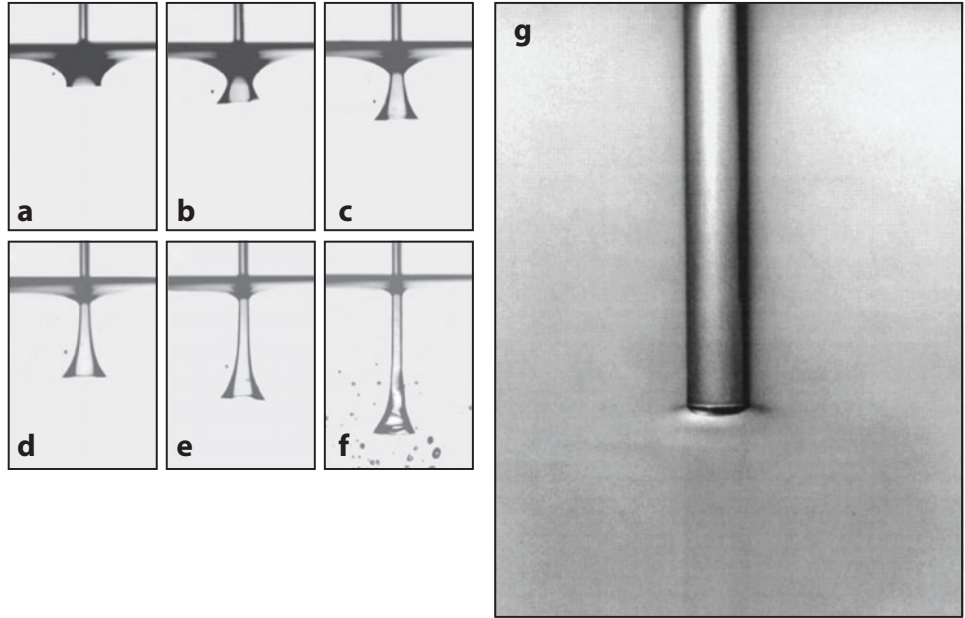


Figure 2

Examples of a laminar meniscus for (a–f) a high-viscosity liquid (silicone oil, $\mu_\ell = 970$ mPa·s, and air, $D_j = 1.5$ mm, with U_j not reported) and (g) a low-viscosity liquid (water and air, $D_j = 6$ mm, $U_j = 3.03$ m s $^{-1}$) Panels a–f taken from Lorenceau et al. (2004) and panel g from Chirichella et al. (2002).

observed cusp formation using a partially immersed four-roll mill, followed by further analytical Stokes flow analysis of the entraining viscous liquid by Jeong & Moffatt (1992). This early work noted that the radius of curvature, r , forming the cusp between the two liquid streams decreases exponentially with the capillary number, namely,

$$r \approx d \exp[-Ca] = d \exp\left[-\frac{\mu_\ell U_j}{\sigma}\right],$$

where d is an external length scale specific to the outer flow region around the cusp. Although Jeong & Moffatt derived this result analytically, the scaling can be constructed by physical arguments based on a balance between surface tension and viscous drag at the tip of a two-dimensional (2D) nascent cusp (Lorenceau et al. 2003). Specifically, the viscous drag per unit length exerted on the tip of the cusp is argued to scale as that of an infinite 2D semicylinder of radius r , which is proportional to $\mu_\ell U / \ln(d/r)$. This viscous force is balanced by the interfacial tension exerted on the cusp by the two (nearly) parallel interfaces attached to it, giving a magnitude of 2σ .

This above scaling, however, does not by itself answer the question of how the critical entrainment condition is attained; it demonstrates only that the radius of curvature decreases exponentially with the capillary number. When neglecting the entrained fluid, one finds that such cusp flows are linearly stable and require finite-amplitude disturbances to perturb them from their steady shape (Jeong & Moffatt 1992). Instead, the steady cusp solution is broken by the viscous pumping of the entrained fluid into the decreasing gap, generating a lubrication pressure that subsequently destroys the force balance responsible for the cusp formation (Eggers 2001). Following this result leads to a critical capillary number for entrainment inception, with a logarithmic dependence on

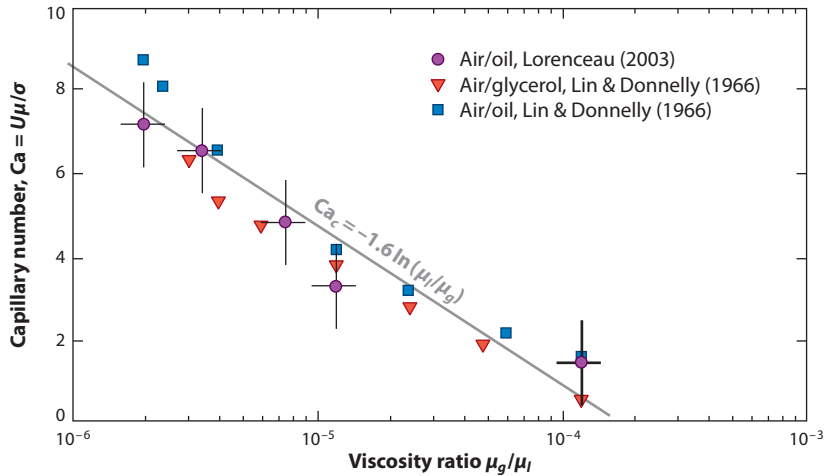


Figure 3

Critical entrainment conditions for viscous jets. Data compiled from Lin & Donnelly (1966) and Lorenceau (2003). The regression line is given by $Ca_c = -1.6 \ln(\mu_\ell/\mu_g) - 13.7$. Figure adapted from Lorenceau (2003).

the viscosity ratio of the two fluids:

$$Ca_e = \frac{U_e \mu_\ell}{\sigma} \propto \ln\left(\frac{\mu_\ell}{\mu_g}\right).$$

Lorenceau (2003) performed several tests of different grades of silicone oil and air and compiled her data with those of Lin & Donnelly (1966) (see **Figure 3**) to produce the regression

$$Ca_e = -1.6 \ln\left(\frac{\mu_g}{\mu_\ell}\right) - 13.7. \quad (4)$$

The similarity to Lin & Donnelly's correlation becomes clear when one notes that the capillary number is simply the product of the Weber number and the inverse of the Reynolds number, giving

$$Ca_e = \frac{We_e}{Re_e} = \left(\frac{\rho U_e^2 d}{\sigma}\right) \left(\frac{\mu_\ell}{\rho U_e d}\right),$$

and thus

$$We_e \propto Re_e \ln\left(\frac{\mu_\ell}{\mu_g}\right). \quad (5)$$

The discrepancy in the exponent of the Reynolds number can be attributed partly to the fact that the viscosity ratio was not considered by Lin & Donnelly, but perhaps more importantly, the above analysis is strictly valid only for flows with no significant inertia. Some of Lin & Donnelly's test conditions occurred up to a Reynolds number of approximately 1,500, at which such effects are likely to be significant.

Under viscous conditions, the thin entrained film is assumed to have a linear Couette profile, with a resulting air-entrainment rate of $Q = \ell_p \delta_{gap} U_j / 2$, where ℓ_p is the perimeter of the jet/pool contact region, and δ_{gap} is the thickness of the entrained film. Lorenceau et al. (2004) argued for scaling laws similar to the Landau & Levich (1942) problem used to determine the thickness of a

viscous film being withdrawn from a pool by a solid plate. They proposed that

$$\delta_{gap} \sim r(\mu_g U_j / \sigma)^{2/3}.$$

This gives an entrainment rate that scales as

$$Q \propto r(\mu_g / \sigma)^{2/3} \ell_p U_j^{5/3}.$$

The above relationship is strictly valid only for small capillary numbers but was observed to fit experimental data over four decades up to $Ca \sim 1$. At larger capillary numbers, it is anticipated that a different scaling law would prevail because of a shift toward a gravitational/viscous balance, giving an air-entrainment rate of $Q \propto U_j^{3/2}$. Unfortunately, no direct tests of this scaling have been reported, although indirect verification is acquired from Lorenceau's work in which she obtained the gas film thickness from a measurement of the entrained air rate.

2.4. Entrainment Mechanisms for Low-Viscosity Jets

The prediction of entrainment conditions for low-viscosity plunging jets is not as straightforward as that for their viscous counterparts, and indeed even defining the criteria for what conditions constitute a low-viscosity jet is not discussed in the literature. Qualitatively, the distinction between these two types in the context of air entrainment appears to result from one of several inertial instabilities that develop in the meniscus region prior to reaching the visco-capillary entrainment threshold discussed in Section 2.3. Thus one may expect the low-viscosity entrainment regimes to occur when the Reynolds number is sufficiently large [e.g., $Re > O(10^2)$], while still maintaining the capillary number below the visco-capillary entrainment threshold [$Ca < O(1)$]. The exact transition between the high- and low-viscosity mechanisms is likely sensitive to the fluctuation level of the oncoming stream (as discussed below in the context of the critical entrainment velocity), but a quick sampling of minimum entrainment conditions in the literature may provide some useful numbers. Based on observations of low-viscosity oil/air systems by El Hammoumi et al. (2002), minimum threshold entrainment values around $Re_e \sim 200$ were observed with a $Ca_e \sim 0.67$. Water and air systems have always been categorized within the low-viscosity regime, with minimal critical air-entrainment conditions occurring for $Re_e \sim 2,000$ with $Ca_e \sim 0.04$, based on data from McKeogh (1978). Given the inverse variation between Re and Ca in these two cases, it may be more useful to think of this boundary between the high- and low-viscosity mechanisms as a Weber number condition, given that $We = ReCa \sim O(10^2)$. This is consistent with entrainment criteria for turbulent short-length jets proposed by Ciborowski & Bin (1972), who proposed that $We_e > 400$.

Because much early work on air entrainment was focused on engineering applications using manmade jets, it was more convenient to eliminate the parameters associated with the impact site in favor of indirect parameters of the nozzle geometry and distance of the orifice from the impact location. Thus the details of the local conditions at the point of entrainment were obfuscated in favor of the geometry of the system design, which folds an additional layer of dynamics due to the evolving liquid jet into the problem (Lin & Reitz 1998). The ramification is that the entrainment criteria were subdivided into cases in which the jet was segregated into a stream of successive closely spaced discrete droplets and those in which it still formed a contiguous ligament. Bin (1993) provided a thorough summary of the data available at the time and correlations for both these regimes. The main conclusions were that (a) the droplet regime criteria were well correlated by a dimensional power law of the Weber number and jet diameter and (b) the continuous jet regime did not lend itself to accurate and reliable inception criteria.

For the droplet impact regime, the correlation suggested by Bin (1988) agreed within $\pm 10\%$ for the majority of the available data, and he put forward the supposition that this entrainment

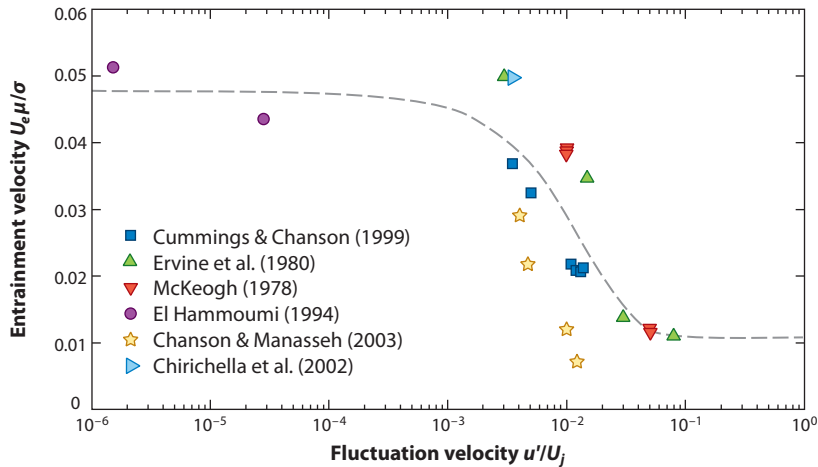


Figure 4

Critical entrainment conditions for low-viscosity fluctuating jets. Figure adapted from Cummings & Chanson (2009).

condition corresponded simply to the jet entering the droplet regime (i.e., the jet entrained air because it had broken into discrete drops). The implication that multiple-droplet impacts always entrain air is interesting, in that single-droplet impacts are known to entrain air only within a narrow range of conditions (Rein 1993). The most important difference, however, is that a jet produces a sequence of multiple interacting impacts, which dramatically alters the free surface motion from the quiescent pool assumed in single-drop impact studies. There also should be a lower bound to when a stream of discrete droplets will entrain air, as at some point the available energy will be insufficient to overcome the resisting forces required to generate the bubble. Indeed, the correlations reported had the greatest scatter for the smallest size diameter, but no lower bound was specifically reported. We further discuss the behavior due to discrete impacts in Section 2.4.3 on highly disturbed plunging jets below.

For the continuous jet conditions, several recent studies have added data to the literature since the review by Bin (1993). High-speed movies of planar jets (Chanson & Manasseh 2003, Cummings & Chanson 1997) showed several regimes of inception behavior for low-viscosity air/water-entrainment conditions: (a) At the lowest speeds ($U_e \approx 0.7 \text{ m s}^{-1}$), entrainment occurred intermittently as discrete bubbles pinched off from the impingement boundary and appeared to correspond to larger disturbances propagating on the jet surface (see schematic in **Figure 1d**); (b) at slightly higher speeds ($U_e \approx 1 \text{ m s}^{-1}$), an unstable air cavity formed at random locations around the perimeter of the impact site, and air was drawn down in larger bursts from the cavity tip (**Figure 1c**); and (c) at higher velocities ($U_e \approx 3.5$ to 5 m s^{-1}), a distinct cavity formed along the entire perimeter, and air was entrained by the breakup of the cavity. Consistent with earlier work (Ervine et al. 1980, McKeogh & Ervine 1981), these inception conditions were inversely proportional to the fluctuation intensity at the impact location, and newer data (Chirichella et al. 2002, Cummings & Chanson 1999, El Hammoumi 1994) were used to develop a dimensionless correlation (Chanson 2009, Cummings & Chanson 1999) for the inception velocity, as shown in **Figure 4**:

$$\frac{U_e \mu}{\sigma} = 0.0109 \left[1 + 3.375 \exp \left(-70 \frac{u'}{U_j} \right) \right]. \quad (6)$$

No physical argument was given to guide its development.

As a last parameter, the influence of translation on the entrainment conditions of a smooth circular jet was studied by Chirichella et al. (2002). They found that the entrainment inception exhibited a Froude scaling such that the critical entrainment condition was given by $Fr_t = V_t(gD_j)^{-0.5} > 1.1$ to 1.4, depending on the impact velocity (where V_t is the translational velocity of the jet). High-speed imaging of the inception conditions showed that the beginning of entrainment resulted from an instability of the cusp created by the low-pressure region in the wake of the translating jet. The instability was correlated with the roll-up of jet vorticity in the upstream side of the submerged jet.

2.4.1. Taxonomy of low-viscosity-entrainment mechanisms. Once the flow conditions have exceeded the inception requirements, it is important to understand what mechanism is established to control the rate of air entrainment. The conditions are broadly divided into several regimes, depending on the viscosity of the working fluid as well as the velocity and disturbance state of the impacting liquid: (a) viscous laminar conditions; (b) low-speed, low-disturbance jets; (c) low-speed, highly disturbed jets; and (d) high-speed jets (Bin 1993, Cummings & Chanson 1997, Kumagai & Endoh 1983, McKeogh & Ervine 1981). The boundaries of the above categories are somewhat arbitrary, with the low-speed region typically categorized as $U_j < 5 \text{ m s}^{-1}$ (Bin 1993), and a gradual transition to high-speed conditions when $We_g = \rho_g U_j^2 D_j / \sigma > 10$ (van de Sande & Smith 1973), although this does depend on the jet characteristics. A visual taxonomy of these conditions is shown in **Figure 2a–f** for regime a; **Figure 5a,b** and **Supplemental Videos 1** and **2** for regime b; **Figure 5c,e,f** and **Supplemental Videos 3–6** for regime c; and **Figure 5d,g,b** and **Supplemental Videos 4, 7, and 8** for regime d (follow the **Supplemental Material** link from the Annual Reviews home page at <http://www.annualreviews.org>).

2.4.2. Entrainment mechanisms for weakly disturbed plunging jets. For low-viscosity cases with a very weak disturbance level (usually no readily visible perturbation to the jet surface), the air-entrainment mechanism has typically been idealized as the growth of an instability on a thin submerged gas film surrounding the perimeter of the jet. This was first treated as a stability problem by Lezzi & Prosperetti (1991), who modeled the flow as a viscous gas layer surrounded by two inviscid liquid regions. They found two modes that were driven by either a long-wave Kelvin-Helmholtz mechanism or a viscosity contrast mechanism at intermediate to smaller wavelengths. The instability growth rates were used to make an order-of-magnitude estimate of the film breakup length for a typical water entry speed of 0.7 m s^{-1} and an assumed gas film thickness of $30 \mu\text{m}$, resulting in a breakup length of 0.4 cm .

In contrast, Bonetto et al. (1994) performed a completely inviscid analysis, assuming stagnant conditions in the outer pool and a thin gap. They found an unstable mode with maximum growth at a wavelength $\lambda \sim 10\sqrt{\sigma/g\rho}$, which for water corresponds to a length of approximately 3 cm . Implicit in both of the above models is that the air-entrainment rate will be governed by gas flow in the film and its subsequent breakup, and hence the thickness of the film is needed. In Bonetto et al.'s model, the gas is stagnant, so the wave speed of the disturbance is used to determine the entrainment rate. A regression to the air-entrainment data of McKeogh & Ervine (1981) is used to extract an effective film thickness of approximately $300 \mu\text{m}$, which is an order of magnitude larger than the estimate used by Lezzi & Prosperetti. In another study, Cummings & Chanson (1997) estimated their sheet thickness from visual observation as varying between 500 to $5,000 \mu\text{m}$.

Although conceptually quite interesting, these models have not been widely utilized to predict air entrainment. This is partly because their validity has only been examined anecdotally in a small set experimental data. Perhaps more significantly, (a) the precise shape of the meniscus depends greatly on the details of the impinging stream and the receiving pool, and (b) visualizations indicate that many entrainment events occur at isolated locations on the meniscus as highly 3D

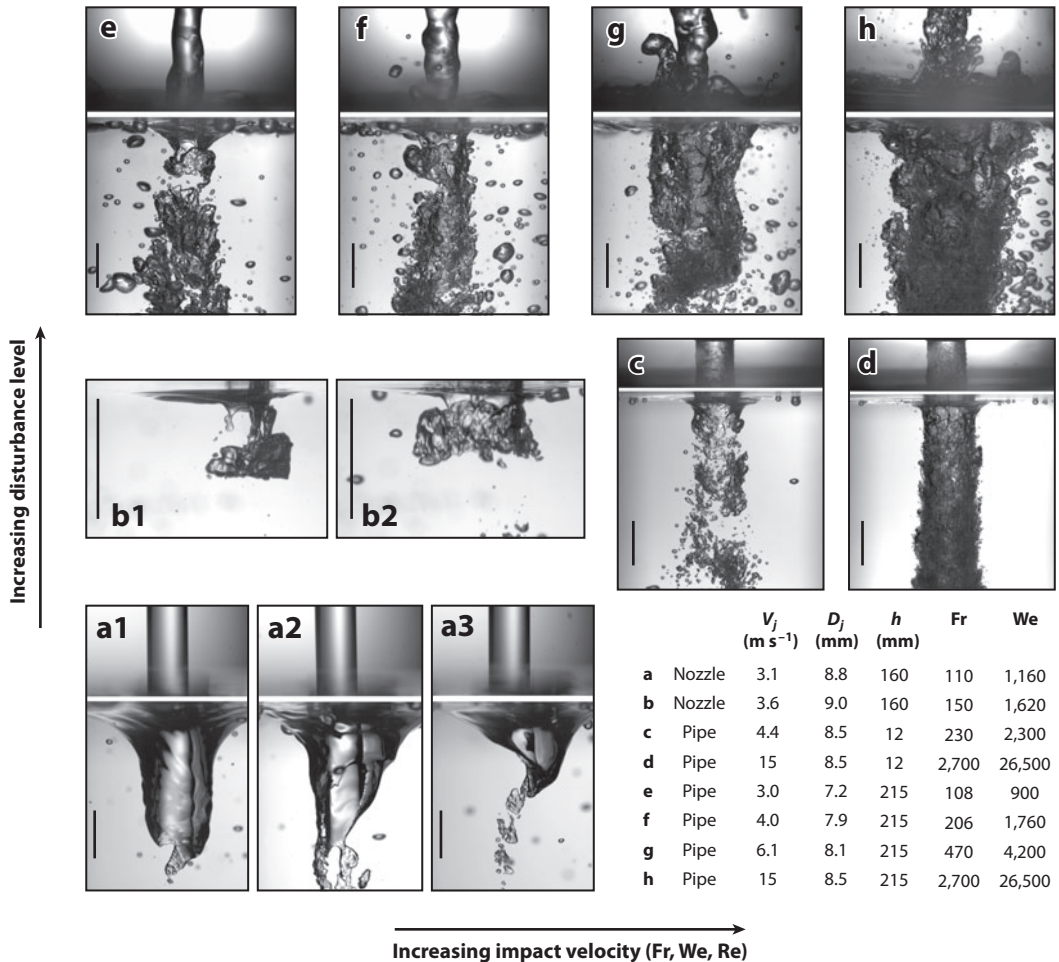


Figure 5

Taxonomy of steady jet air-entrainment conditions. The black line indicates a 10-mm length reference. In cases *a* and *b*, the jet was produced by a smoothly contoured nozzle, and in cases *c*–*h*, a smooth brass pipe of length $L/D_o = 100$ was used to ensure fully developed turbulent flow prior to the exit. The images in panels *a1*–*a3* were acquired at under the same conditions but at different points in time. The images in panels *b1* and *b2* likewise show two different entrainment bubbles from the same test. All panels (except *b*) show a simultaneous view of the above surface jet and the below-surface air entrainment. For movies corresponding to several of these, readers are referred to **Supplemental Videos 1–8**.

 **Supplemental Material**

destabilizations and only occasionally resemble 2D breakage events. These points can be exemplified by the variability of the local inflow conditions under the so-called intermittent vortex regime (McKeogh & Ervine 1981). In this case, an axial vortex is formed in the receiving pool, resulting from an amplification of strained vorticity entrained from the bulk fluid. The strength of the circulation and the location of its axis vary with time, and when it aligns with the meniscus, the combined low pressure of the vortex core and that induced by the entrainment from the jet are sufficient to generate an asymmetric and deep inverted meniscus (sometimes several jet diameters), from which bubbles are entrained from the tip (**Figure 5a**). At times, the meniscus does in fact appear to destabilize over an extended edge of the lip in a quasi-2D fashion, but this quickly evolves into a more concentrated 3D air stream.

At higher speeds, the intermittent vortex regime is not as prevalent, and more sites around the periphery actively entrain air, giving the appearance of a continuous sheet breakup (Bonetto & Lahey 1993, Brattberg & Chanson 1998), which has been likened to that of a ventilated cavity (Cummings & Chanson 1997). Closer inspection of these conditions, however, shows that frequently air is transiently entrained by one or more stems or fingers that rapidly expand at their end, filling in along the lateral directions of the flow (see **Figure 6**). This is most often accompanied by a rotational motion about the azimuthal axis, as evidenced by occasional folding of the forming bubble and the motion of smaller bubbles entrained in the vicinity. This gives the appearance that a structure of the subsurface jet, such as a large-scale vortex ring, is responsible for destabilizing the meniscus, as put forth schematically by Oguz et al. (1992), shown in the translating-jet case (see **Figure 7**) by Chirichella et al. (2002) and suggested by the unsteady viscous finite-element simulations of Galimov et al. (2010). The more intense entrainment events are often associated with slight disturbances in the jet surface (Cummings & Chanson 1999), which may be responsible for generating such organized structures in some cases. Indeed, a similar idea was put forth by Oguz (1998), who studied the entrainment by a moderate speed jet ($U_j = 3.7$ to 8.1 m s^{-1}) within a confined annular gap. The confined air film was found to be unstable to small-amplitude disturbances generated by a turbulent boundary layer within the jet nozzle, once the disturbances exceeded a critical Weber number of $We_c > 4$, with the length scale specified as the amplitude of the disturbance. The role played by subsurface disturbances is discussed more fully in Section 2.6.

Finally, the presence of bubbles or foam entrained into the meniscus region from the pool surface can potentially destabilize the meniscus and trigger entrainment events (Cummings & Chanson 1999). Some authors have also suggested that the air boundary layer surrounding the jet can be a contributing factor. However, a quick check indicates that this likely plays only a minor role until one reaches higher speeds, as even for moderate-speed jets ($U_j \sim 5 \text{ m s}^{-1}$), the stagnation pressure is sufficient only to depress the water surface by 1.5 mm. At higher velocities at which the boundary-layer effect may be relevant, the liquid free surface is typically disturbed by the shear from the gas stream, restricting its relevance to the high-velocity and/or highly disturbed conditions (Evans et al. 1996, McKeogh & Ervine 1981).

Fundamental work on translating jets has been reported by Chirichella et al. (2002), who documented the entrainment boundaries produced by a laminar axisymmetric steady jet translated over a quiescent pool. Although they found that the entrainment boundary was caused by forcing from vorticity generated by the impinging jet, the continuous regime of air entrainment was quite similar to the intermittent vortex mechanism noted above. In this condition, air was entrained in a fairly steady stream emanating from the cusp of the cavity created in the downstream wake of the impacting jet (see **Figure 7c**).

2.4.3. Entrainment mechanisms for highly disturbed jets and transient impacts. For highly disturbed impacting jets, the incoming stream becomes nonuniform, characterized by a visibly rough surface with wavelengths varying from those dictated by capillary-shear balance up to the size of the jet, depending on the development length prior to impact (Lasheras & Hopfinger 2000, Villermaux 2007). If given sufficient time, the incoming stream will break up into a series of discrete drops or lumps, leading to a transient impact process. The transient impact also occurs as a result of the starting process of a continuous stream and occurs commonly in breaking waves. Here we focus on recent contributions to what is known about transient impacts followed by entrainment from highly disturbed jets and the connection between the two.

Starting with the impact of a finite volume of liquid onto a receiving pool, the simplest case is when the liquid is in the form of a sphere. This corresponds to the case of drop impact, as reviewed by Rein (1993) and explored in the studies of Pumphrey & Elmore (1990) and Oguz &

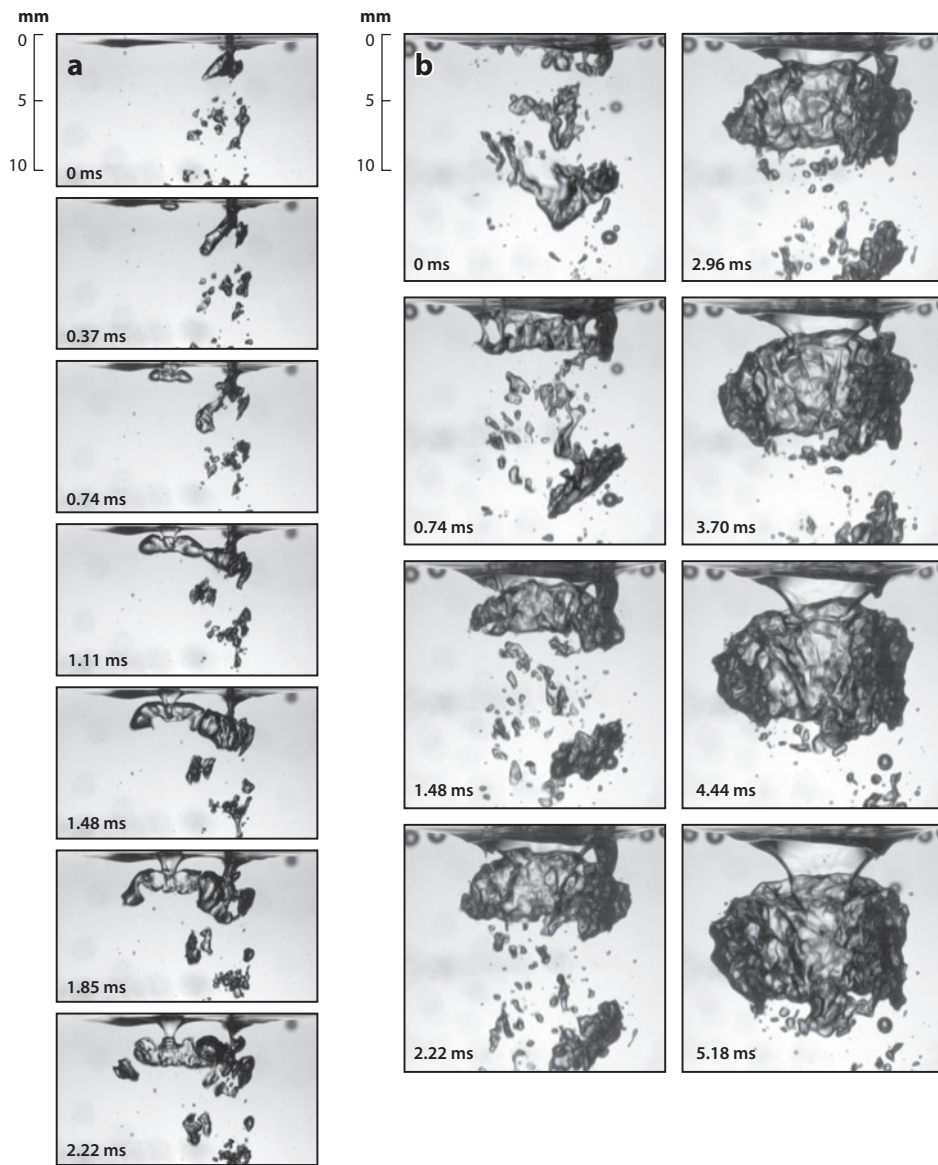


Figure 6

Sequences of individual air-entrainment events from a weakly disturbed jet (conditions correspond to those in **Figure 5b**; $U_j = 3.6 \text{ m s}^{-1}$, $D_j = 9 \text{ mm}$, and $h = 160 \text{ mm}$): (a) sequence showing entrainment from two stems to form a smaller azimuthally oriented bubble and (b) sequence showing entrainment from initially many stems that quickly join to form a continuous sheet, rapidly filling a large bubble.

Prosperetti (1990). The initial impact of the fluid generates an expanding hemispherical crater in the pool, typically rimmed by a splash. The growth of the crater is counteracted by the ambient hydrostatic pressure, which eventually reverses the crater wall motion and causes the cavity to collapse. Perhaps contrary to intuition, this geometry entrains air only over a narrow range of droplet diameters and velocity conditions. The boundaries of the air-entrainment regime are

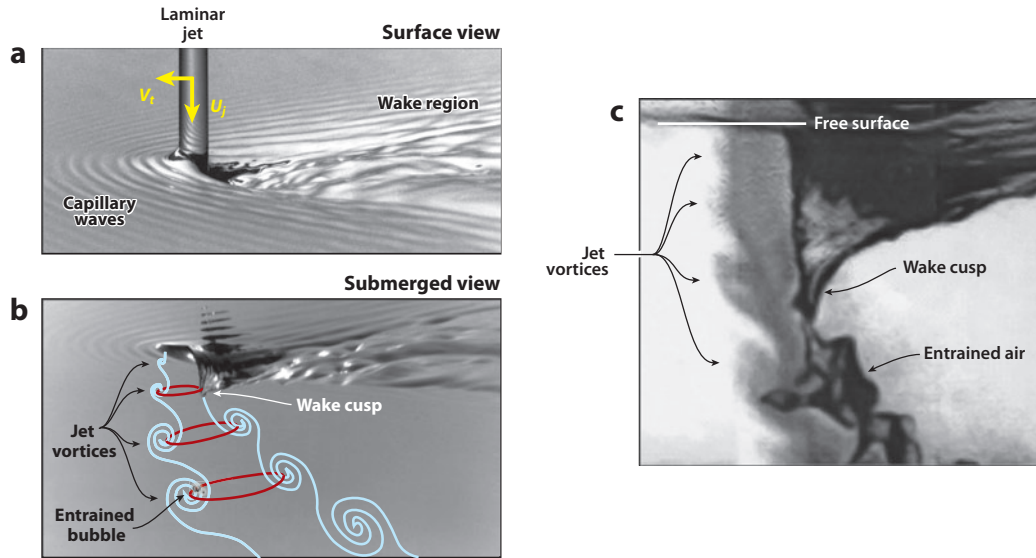


Figure 7

Schematic of air entrainment by a cylindrical translating jet. (a) Above surface and (b) submerged view of laminar translating jet near incipient entrainment conditions ($D_j = 0.65$ cm, $U_j = 298$ cm s⁻¹, and translation velocity $V_t = 35.6$ cm s⁻¹). (c) Submerged view of continuous entrainment conditions ($D_j = 0.57$ cm, $U_j = 237$ cm s⁻¹, and translation velocity $U_t = 38.1$ cm s⁻¹). In panel c, the jet was marked with dye, revealing the location of large-scale jet vorticity. Figure modified from Chirichella et al. (2002).

controlled by the reversal of the downward surface motion at the bottom of the crater prior to the inward collapse of the crater walls, all of which is subtly modulated by the effects of surface tension. The result leads to a $We_e \propto Fr_e^{1/4}$ and $We_e \propto Fr_e^{1/5}$ scaling (where the Weber and Froude numbers are based on the diameter and speed of the droplet just before impact) for the upper and lower entrainment boundaries, respectively, as observed experimentally by Prosperetti et al. (1989) and later in numerical simulations by Oguz & Prosperetti (1990). This is referred to as the regular entrainment regime, as it is a condition under which air is reliably entrained. Two other regimes, denoted as irregular (Pumphrey et al. 1989) and vortex ring (Carroll & Mesler 1981, Rodriguez & Mesler 1988), have also been identified but entrain air only infrequently.

In the case in which the droplets come from a disintegrating jet, it is likely that multiple impacts may occur within quick succession, with much different entrainment criteria than that observed for the isolated-droplet case (Bick et al. 2010, Franz 1959). Specifically, for small-diameter water jets, it was found that air entrainment was possible across a similar Froude number range to the single-drop case, but with an order-of-magnitude-smaller Weber number, provided a second drop impact occurred within a critical time dictated by the capillary timescale of the preceding drop (associated with the impact crater recovery) (Bick et al. 2010). The preceding study was limited to smaller drop sizes, and hence it is not clear what boundaries may exist, if any, as the drop size is increased. The previously noted tendency for jets to entrain air as soon as they reach their break-up length would seem to indicate that multidrop entrainment may occur for a continuous range of drop sizes and velocities once beyond a critical capillary scale, although the mechanism would likely switch to a gravitationally driven closure mechanism at larger sizes.

Changing the geometry of the impacting mass to an axisymmetric column forms the basis for studying air entrainment by short duration jets, with an approximation of the drop case being

recovered when the aspect ratio of the column is close to unity (albeit a nonspherical droplet). Kolaini et al. (1991, 1993) considered experimentally the problem of a short-duration water jet impacting on a quiescent pool of water, which was subsequently modeled and simulated numerically by Oguz et al. (1995). An elegant scaling argument was constructed on the basis of these results, using a potential flow Rankine body as the source of radial momentum to form the cavity, counteracted by a local time-dependent gravitational collapse. The results lead to a pinch-off depth that scales as $H_c = \frac{3}{2} D_j Fr^{1/3}$, at a pinch-off time $t_c = 6(D_j/2g)^{1/2} Fr^{-1/6}$, and the volume of entrained air

$$\frac{\Phi}{D_j^3} \propto Fr^{1/3}. \quad (7)$$

Studies performed on smaller diameter jets (Kersten et al. 2003) indicated that surface tension and Reynolds number effects can have a significant influence on this result, causing an increase in the pinch-off depth in comparison to the expected inviscid scaling arguments. Later work by Soh et al. (2005) provided an integral analysis of the impact, predicting that the maximum depth of the cavity varies as $Fr^{1/3}$ to leading order, in agreement with prior work.

The entrainment of a translating impact of a planar jet was studied by Gomez-Ledesma et al. (2011), who documented the pinch-off time and pinch-off depth of the transient cavities formed by the impact while varying the translation velocity, impact angle, impact velocity, and jet thickness. They found that increasing the translation velocity decreased the pinch-off depth and pinch-off time, and a simple quasi-steady potential flow model similar to that of Oguz et al. (1995) was used to predict the cavity formation and collapse. The model gave similar results to the experiment in all cases except those with shallow impact angles, which was speculated to result from the proximity of the crater to the free surface and/or the breakdown of the quasi-steady analysis constraint. One interesting result from the simple model was that for a steady-state solution to occur with a penetrating translating jet, the translation velocity magnitude must not exceed the impact velocity of the jet, $V_t < U_j$, which may not be satisfied in some applications.

The above studies were further augmented by considering the case of an initially nonentraining plunging jet perturbed by a small surface undulation (Ohl et al. 2000, Zhu et al. 2000), which has provided insight into the mechanisms of how air entrainment is established in highly disturbed low-velocity jets. These studies produced both experimental and numerical observations of the disturbance growth propagating along the jet, as well as the cavity generated by the bump. Upon contact of the disturbance with the receiving pool, an initial crater was formed similar to that created by an impacting droplet (**Figure 8**). In contrast to the droplet case, however, the presence of the jet encouraged the formation of a thinner secondary sheath or cavity of air extending from the bottom of the crater. It was this secondary cavity that would subsequently pinch off and form a submerged bubble, similar to the case created by a falling cylindrical mass of liquid (Oguz et al. 1995). Consequently, the scaling of the entrained air volume also follows an $Fr^{1/3}$ relationship. Tracking the energetics of the disturbance indicated that the momentum of the jet was being utilized to augment the air entrainment relative to an equivalent, similarly sized droplet and that the air-entrained volume, Φ , scaled with the size of the disturbance. Specifically, they found that for their limited set of conditions at a single Froude number ($Fr = 52$),

$$\left. \frac{\Phi}{D_j^3} \right|_{Fr=52} = 6.7 \left(\frac{D_b}{D_j} - 1.15 \right). \quad (8)$$

As noted by Ohl et al. (2000) and Kersten et al. (2003), this has interesting implications for the entrainment of air by highly disturbed water jets, in that one may view the large-amplitude

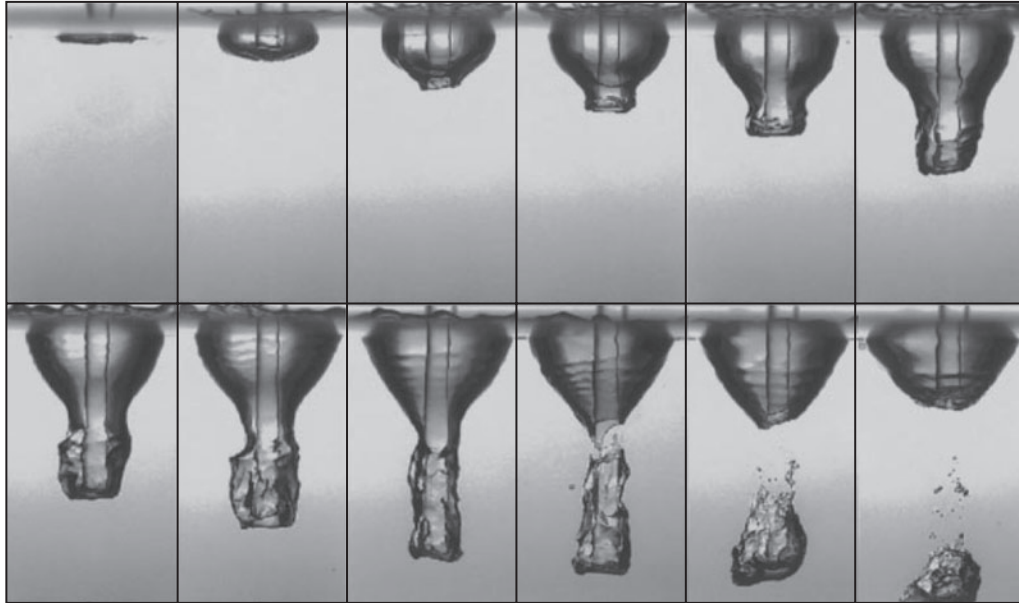


Figure 8

Air entrainment by a single disturbance or bump on a nonentraining, laminar jet ($Fr = 52$, $We = 260$). Figure taken from Zhu et al. (2000).

disturbances as a succession of bumps impacting the receiving pool. Indeed, visualizations of disturbed jets shown in **Figures 5** and **6** depict sequences similar in form to those produced by an isolated disturbance (**Figure 8**). The main differences seem to be that the isolated-disturbance case produces a much longer and narrow cavity deeper into the flow, whereas in the randomly disturbed case, the cavity is rapidly concentrated into a local semiannular space. This likely results from the higher-Weber number conditions in the disturbed jet as well as the significant asymmetry present in the flow. The formation of a cavity along only a portion of the submerged jet will allow it to interact strongly with the vorticity rolling up from the penetrating jet. This mode of air entrainment appears prevalent from low to moderate impact speeds, but at high speeds (in excess of $\sim 7 \text{ m s}^{-1}$), the continual impact of the bumps sweeps out a much deeper cavity that appears as a persistent biphasic layer.

2.5. More Recent Air-Entrainment-Rate Models

Since the comprehensive review by Bin (1993), several new correlations for the air-entrainment rate by steady jets have been published for high-speed confined jets (Evans et al. 1996), low- to moderate-speed jets (Brattberg & Chanson 1998, Ma et al. 2009), and low-speed laminar and turbulent jets (El Hammoumi et al. 2002). For the high-speed conditions of Evans et al. (1996) ($7.8 < U_j < 15 \text{ m s}^{-1}$), the authors proposed a multizone model based on the combined entrainment from a thin gas film surrounding the jet and gas pockets trapped within of the disintegrating jet. The correlation was found to fit the data within approximately 20% and is similar to earlier models proposed by Burgess & Molloy (1973), McKeogh & Ervine (1981), and van de Sande & Smith (1973), which show a similar level of agreement, as summarized by Bin (1993).

The three correlations by Brattberg & Chanson (1998), Ma et al. (2009), and El Hammoumi et al. (2002) overlap in their respective impact conditions and merit comparison when cast in similar form. For the comparison, the correlations are listed in the form of an air-/liquid-entrainment ratio with the explicit dependence on the jet impact velocity highlighted. For El Hammoumi et al. (2002), their original dimensionless groups give

$$\frac{Q_a}{Q_l} = \begin{cases} 6.0 \times 10^{-5} \frac{\rho_l^{0.418} \sigma^{0.818}}{\rho_a^{0.5} \mu_l^{0.735} g^{0.16}} b^{0.695} D_o^{-0.89} U_o^{-0.58} & \text{Re}_o < 2,300 \\ 9.2 \times 10^{-2} \frac{\rho_l^{0.022} \mu_l^{1.3}}{\rho_a^{0.5} \sigma^{0.817} g^{0.45}} b^{0.885} D_o^{-1.81} U_o^{1.23} & \text{Re}_o > 3,200 \end{cases}, \quad (9)$$

where b is the fall height from the nozzle to the receiving pool. The work of Brattberg & Chanson (1998) is in its original form:

$$\frac{Q_a}{Q_l} = \begin{cases} 7.7 \times 10^{-4} \left(\frac{b}{D_j} - 1.04 \right) \left(\frac{U_j - U_e}{\sqrt{g D_j}} \right)^{1.8} & \text{for } U_e < U_j < 4 \text{ ms}^{-1} \\ 2.0 \times 10^{-3} \left(\frac{b}{D_j} - 1.04 \right) \left(\frac{U_j - U_e}{\sqrt{g D_j}} + 9.3 \right) & \text{for } 4 < U_j < 8 \text{ ms}^{-1} \end{cases}, \quad (10)$$

and for the work of Ma et al. (2009) reduces to

$$\frac{Q_a}{Q_l} = K_2 \times \begin{cases} \frac{U_j^2}{g D_j} & \text{for } 1 < \frac{U_j}{U_e} < \frac{U_t}{U_e} \\ \left(\frac{U_t^2}{g D_j} \right)^{\frac{3}{4}} \left(\frac{U_j^2}{g D_j} \right)^{\frac{1}{4}} & \text{for } \frac{U_t}{U_e} < \frac{U_j}{U_e} \end{cases}, \quad (11)$$

where $U_t = 4.5 \text{ ms}^{-1}$ is noted as the transition velocity between the two regimes. From the above, a similar dependence on the jet velocity is observed in comparison to Equation 10, namely an approximate quadratic dependence on the jet impact velocity ($Q_a \propto U_j^{1.8}$ and U_j^2 for Equations 10 and 11, respectively) for the low-speed case, with a decreased exponent ($Q_a \propto U_j^{1/2}$, U_j^1) for the higher-speed transitional case. The turbulent case of El Hammoumi et al. (2002) in Equation 9 is comparable to the higher-speed transitional conditions of Equation 10 and 11, with $Q_a \propto U_j^{1.23}$. The laminar condition of El Hammoumi et al. (2002) (Equation 9), on the other hand, is quite different from the other correlations. Although the exit conditions are stated as laminar in their tests, it is not clear what entrainment behavior was exhibited at the impact location for these test conditions. The authors noted a fair bit of scatter even within their own data (45%), and it may be that the conditions were a mix of intermittent vortex (**Figure 5a**) and disturbance-induced (**Figure 5b**) behaviors, which have qualitatively different entrainment mechanisms. Another reason for possible differences is in the treatment of the jet-development length and the parametric range over which the data were fitted. Brattberg & Chanson (1998) and El Hammoumi et al. (2002) retained the free jet length as an explicit variable in their fitting methods and likewise limited their conditions to shorter fall distances ($4.2 < b/D_j < 13.2$ and $14.5 < b/D_o < 82$, respectively), whereas Ma et al. (2009) had more than half of their fitting data from longer fall conditions ($b/D_j > 50$) and incorporated variances in this parameter with a unique constant for each test.

When compared with the previous literature, similar trends can be found for the velocity dependence and jet length dependence, going back to the early work of van de Sande & Smith

(1976), who gave the dimensional correlation

$$\frac{Q_a}{Q_l} \propto \begin{cases} \rho_l U_j^2 & \text{for long jets, } b/L_b > 1 \\ \frac{b^{1/3} U_j}{D_j^{1/2}} & \text{for short jets, } b/L_b < 1 \end{cases}, \quad (12)$$

where L_b is the break-up length of the jet. The long jet conditions provide a similar velocity scaling for the low-speed conditions of Ma et al. (2009) and Brattberg & Chanson (1998), which is somewhat surprising for the latter, given their short jet length ($b/D_j < 13$). The short jet conditions also correspond closely to the transition conditions proposed by both Brattberg & Chanson (1998) and El Hammoumi et al. (2002), but with a weaker dependence on the jet length. Another useful correlation for these conditions was proposed by Bin (1993), valid for a range of jet lengths ($b/D_o < 100$) issuing from long cylindrical pipes ($\ell_{\text{pipe}}/D_o > 10$):

$$\frac{Q_a}{Q_l} = 0.04 \left(\frac{b}{D_o} \right)^{0.4} \left(\frac{U_j^2}{g D_j} \right)^{0.28}. \quad (13)$$

The above correlation predicted other authors' data (van de Sande 1974) across the different regimes within 20%. The correlation systematically overpredicted the entrainment rate for short nozzles, which also showed a steeper dependence on the independent variables (Bin 1993). In comparison with more recent work, this form is most similar to the transitional regime shown in Equation 11, which also exhibited a fractional dependence on $\text{Fr}^{0.25}$. As noted above, all other dependencies were contained in the normalization constant.

2.6. A Mechanistic Cartoon of Entrainment in Low-Viscosity Plunging Jets

Within the above discussion, there are still several unanswered questions and discrepancies concerning air-entrainment thresholds and entrainment rates within plunging jets. Although correlations seem to point to several common trends, it may be helpful to explore additional mechanistic explanations to guide future directions for research. Chief among these would be (a) the role of subsurface vorticity in the entrainment processes and (b) an explicit connection between the single idealized bump of Oguz et al. (1995) and continuous entrainment models. It should be noted that the above two points are not independent: The velocity disturbance created by the motions of the jet surface will likely strongly influence the organization of the subsurface vorticity, when present.

2.6.1. Influence of subsurface vorticity in plunging jet air entrainment. With regard to the role played by the subsurface vorticity in entraining air, above we note that **Figures 5b** and **6** seem to hint at significant rotational motion influencing the entrainment of air in weakly disturbed jet conditions. Inspired by this observation, one may examine the magnitude of forces developed by the subsurface flow and see how they scale relative to the restoring forces of surface tension and gravity, as illustrated schematically in **Figure 9**. Key to this idea is the existence of a shear layer in which the impinging jet separates from the meniscus and rolls itself up into a concentrated vortex through the Kelvin-Helmholtz instability. These vortices then grow through subsequent pairing events as the layer evolves. We note that the existence of a concentrated blob of vorticity is essential, as this generates a local pressure minimum in the core of the vortex, which can act as a driving mechanism to entrap air. Setting up a stress balance in the region around such a vortex, one finds

$$\Delta p_v \propto \frac{\sigma}{R_b} + \rho g z. \quad (14)$$

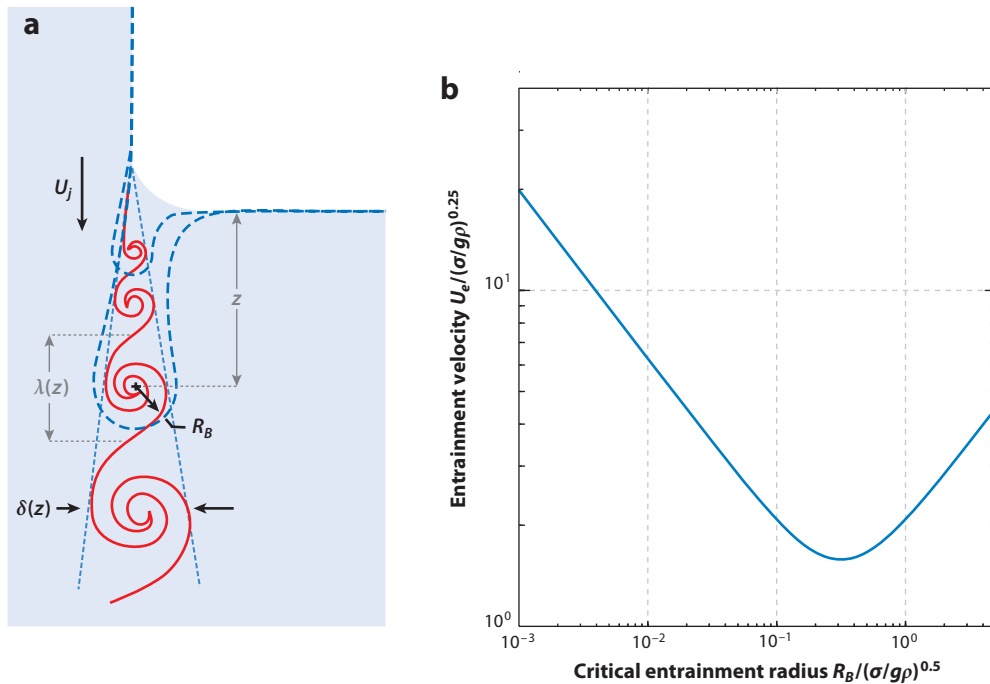


Figure 9

(a) Schematic of the proposed vortex entrainment model and (b) the critical entrainment condition given by Equation 16 for air/water systems.

To capture this effect, one can model coherent rollers as a viscous core Rankine vortex with a radius R_v . The pressure difference between the vortex center and the far field is given by

$$\Delta p_v = \rho \left(\frac{\Gamma}{2\pi R_v} \right)^2 = \rho \left(\frac{U_j \lambda}{2\pi R_v} \right)^2, \quad (15)$$

where Γ is the circulation of the vortex, which can be approximated by the vorticity accumulated over a wavelength λ . Although an oversimplification in the near field, unforced mixing layers grow linearly with distance, with the thickness of the layer given by $\delta \sim \alpha z$ (with typical values of $\alpha \approx 0.2$). The wavelength of the coherent structures is found to be $\lambda \sim 5\delta$ (Winant & Browand 1974). Taking the radius of the vortex and the radius of the entrained bubble to be half the layer thickness, $R_v = R_b = \delta/2$, the critical velocity required for entrainment would be

$$\frac{U_e}{(\sigma g / \rho)^{1/4}} = \frac{\pi}{5} \sqrt{\frac{\ell_c}{R_b} + \frac{2R_b}{\alpha \ell_c}}. \quad (16)$$

where $\ell_c = \left(\frac{\rho g}{\sigma}\right)^{1/2}$ is the capillary length. Equation 16 is plotted in **Figure 9**, where it predicts the general trend of a minimum threshold velocity. Using the above estimates for the conditions of air and water, the minimum critical entrainment velocity is 0.25 m/s, which is approximately three times lower than what is observed, but a similar order of magnitude. It should also be kept in mind that the relationship stems from a static balance and does not account for the required dynamics necessary for the unsteady flow to draw in a moving meniscus. Moreover, this simplified model

does not account for variability in local meniscus shape, which can vary dramatically in laminar and slightly disturbed conditions depending on the receiving pool state, as shown in **Figure 5a,b**.

Finally, the above does not explicitly express the influence of velocity fluctuations within the incoming jet, which are known to have a significant effect. These fluctuations would play a role, however, in altering the roll-up of the shear layer, which is highly receptive to small-amplitude forcing and can dramatically alter the size and wavelength relationships of the vortices (Ho & Huerre 1984). This provides a connection to the bump-entrainment mechanism examined in Section 2.4.3, as such details may be relevant to controlling how much of the jet energy is available to do work against the free surface and are worthy of further investigation. It has been noted that laminar (or small-disturbance-level) low-viscosity jets have a critical entrainment velocity much higher than their high-disturbance counterparts. At low speeds and very high disturbance levels, the irrotational transient bump studies of Zhu et al. (2000) show that a minimum critical bump size is required for air to be entrained. Although the authors examined the minimum bump threshold only for a single Froude number condition, that the maximum volume entrained scales with $Fr^{1/3}$ may hint at a decreasing minimum bump size (and hence disturbance level) as the impact velocity is increased. They suggested that the bump size may play a role in how much of the jet kinetic energy is utilized for expanding the subsurface cavity, but the details of how this happens remain to be explained. Similar to this are the small-disturbance conditions noted by Oguz (1998), who proposed a critical Weber number based on the disturbance size. Thus as the speed increases, a smaller amplitude is needed to destabilize the jet. Corroborating indicators of the above behavior can be seen in the visualizations of Chirichella et al. (2002), the simulations of Galinov et al. (2010) and **Figure 6**. Such mechanisms are not so obvious when comparing the entrainment images of the single-bump perturbations of Zhu et al. (2000) shown in **Figure 8** with those shown in **Figure 5b,c**. In the former work, there does not appear to be as strong a rotational component influencing the entrained sheath, although disturbances are visible that generate cusps and capillary waves along the surface. This likely results from the differences in the Weber number between the two cases ($We = 202$ versus 1,620 and 2,300, respectively), preventing the vorticity from playing a significant role in the smaller- We case. It is also worth noting that in realistic conditions, the disturbances have only limited symmetry, and many events destabilize only over a fraction of the perimeter but can be subsequently expanded azimuthally, as shown in **Figure 6a,b**.

2.6.2. Extension of the single-bump model to continually disturbed jets. It is of interest to explore the suggestion of Zhu et al. (2000) and attempt an air-entrainment scaling based on their bump mechanism. The starting point would be to consider the disturbed jet as a spectrum of individual bump disturbances, which are dictated by the inflow conditions, liquid/air shear, surface tension, and development length. If we limit the discussion for now to long-wave disturbances (laminar jets, longer development lengths), the frequency of bump generation would be $f \propto U_j/D_j$, and the air-entrainment rate would be $Q_a \propto \Phi f$. Generalizing the trends reported by Zhu et al. (2000) to give the bump-amplitude dependence of the volume of air entrained by simply combining Equations 7 and 8, we obtain

$$\Phi = D_j^3 K_3 \left(\frac{D_b}{D_j} - K_4 \right) Fr^{1/3}, \quad (17)$$

giving

$$\frac{Q_a}{Q_i} = K_5 \left(\frac{D_b}{D_j} - K_4 \right) Fr^{1/3}. \quad (18)$$

The resulting simplistic equation is quite similar to Equation 13 proposed by Bin (1993) and the higher-speed conditions of Ma et al. (2009), showing a similar dependence on the Froude number.

Provided one can make a relationship between the bump size and evolution distance of the free jet, both expressions have more similarity, save the exponent. For short jets, the disturbance growth is approximately linear, suggesting a linear dependence on b . The model is in conflict with the low-speed regime of Brattberg & Chanson (1998) and Ma et al. (2009) and the long-jet correlation of van de Sande & Smith (1976), which exhibit a nearly linear dependence on the Froude number. This likely results from the simple dependence on the frequency and symmetry of the disturbances that was assumed, as the case for real jets deviates from this significantly. Incorporating a more sophisticated model of threshold disturbances could lead to an effective intermittency model (as the jet speed increases, more completely formed toroidal bubbles are produced, and with increasing frequency), which might account for the increased exponent associated with the Froude number.

3. APPLICATION TO PLUNGING BREAKING WAVES

One reason to study relatively simple air-entraining flows such as plunging jets is the hope of gaining some insight into entrainment mechanisms in more complex flows. One such flow in the high-Reynolds number regime is plunging breaking waves, which are of considerable importance in geophysics and in particular in air-sea interactions and surf-zone dynamics. In the following, we discuss the mechanisms at work in this complex air-entrainment process and compare them, where possible, to the basic entrainment mechanisms discussed above. The later evolution of void fraction and bubble size distribution is touched on only briefly where it is important for understanding the physics of the flow.

In a plunging breaker, air entrainment occurs by several mechanisms (see **Figure 10**): The entrainment of a tube of air at the instant the plunging jet hits the front face of the wave

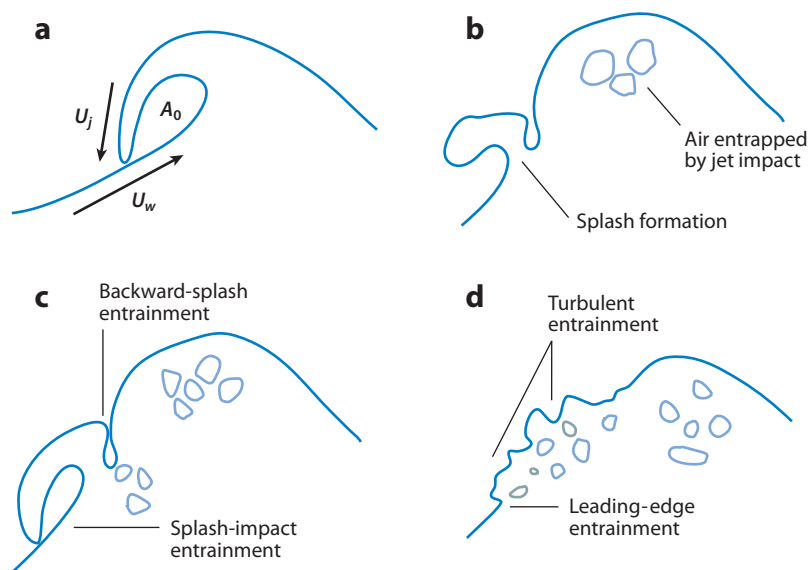


Figure 10

Schematic of air-entrainment mechanisms in a plunging breaker. A_0 is the area of the region of air enclosed at the moment of jet impact, whereas U_j and U_w are the velocities of the tip of the plunging jet and the fluid in the front face of the wave at the jet impact site, respectively, at the moment just before jet impact; both velocities are measured in a reference frame moving with the wave crest.

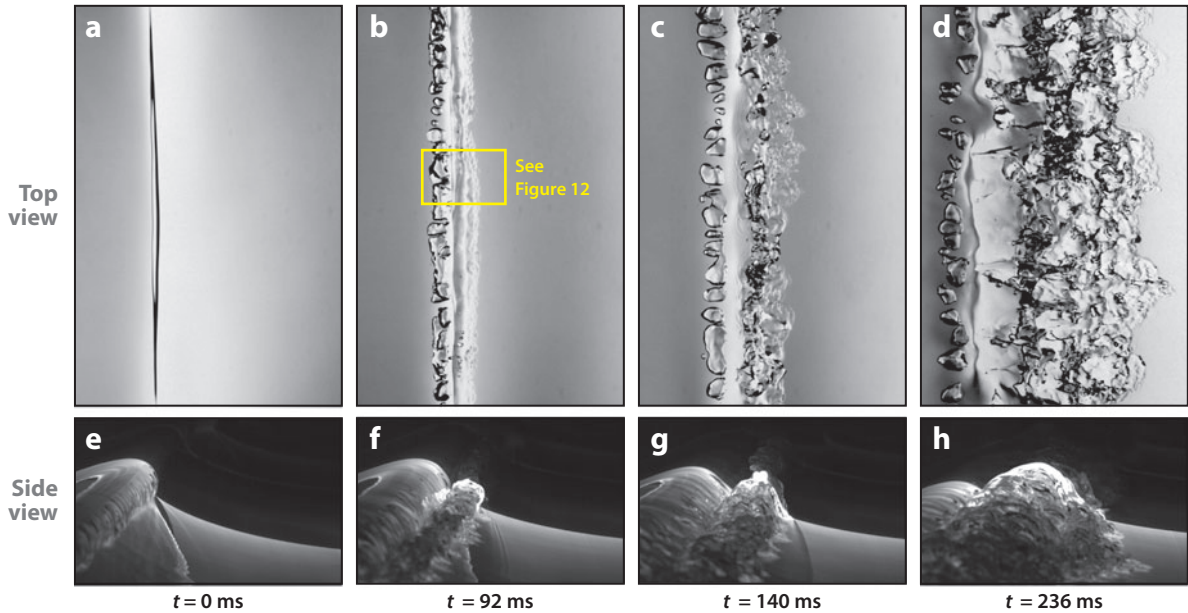


Figure 11

Photographs from high-speed movies of a laboratory-scale plunging breaking wave. The wave was mechanically generated using a dispersively focused wave packet with a nominal wavelength $\lambda = 1.2$ m, and the crest is moving from left to right in the laboratory reference frame. Panels *a–d* are imaged from above the wave crest and illuminated from below, and panels *e–h* were imaged from the side slightly above the waterline to highlight the wave profile. The top and side views are from the same wave conditions but different wave runs (not simultaneously imaged). In all images, the field of view is 16 cm in the direction of wave propagation. A movie of these image sequences is provided in **Supplemental Video 9**.

Supplemental Material

(**Figure 10a**), entrainment around the jet impact site (as the jet drags air into the water) (**Figure 10b**), entrapment by subsequent impacts of forward splashes created by the jet impact (**Figure 10c**), entrainment between the backside of the splash and the upper surface of the plunging jet (**Figure 10c**), entrainment all over the splash and the turbulent breaking regions when the surface bursts into ligaments and droplets in highly energetic or long-wavelength waves, and entrapment at the leading edge (toe) of the turbulent breaking region in the late stages of the breaking process (**Figure 10d**). The latter two mechanisms are also important in long-wavelength/energetic spilling breakers. **Figure 11** shows four pairs of images from top-view and side-view high-speed movies of a weak plunging breaker. The weak plunger was chosen to have only moderate air entrainment and thus to allow better visualization of the entrainment processes. The images in **Figure 11** and the companion images in **Figure 12** are used in the following discussion to illustrate the characteristics of the entrainment mechanisms.

The entrainment of the tube of air under the crest is the most visible and best-understood entrainment mechanism in breaking waves and is depicted in the schematic of **Figure 10a** and the photographs of **Figure 11a,e**. (When interpreting the top-view images in **Figures 11** and **12**, it should be kept in mind that refraction caused by the curved water surface may distort or even block the view of some bubbles and most likely reduces the apparent size of the air tube in **Figure 11a**.) This entrainment process is markedly different than in the transient jet impact experiments discussed in Section 2, in which the impact of the jet tip or a disturbance on the jet creates a large subsurface crater that subsequently collapses below the mean water surface to

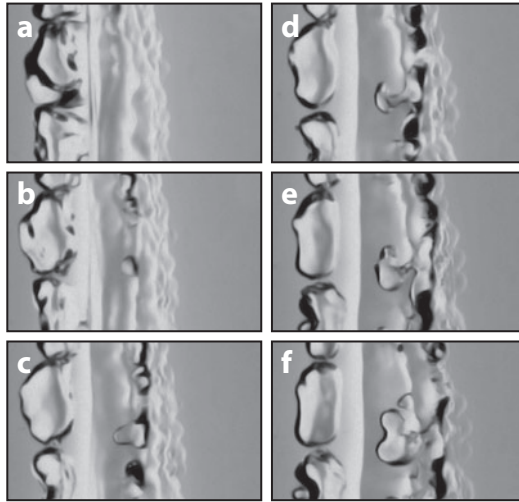


Figure 12

Sequence of images of the region marked by the yellow rectangle in **Figure 11b** showing the entrainment of a bubble near the leading edge of the turbulent breaking region. The horizontal field of view is 5.4 cm in each image. The time between images is 4 ms.

entrain air. In the plunging breaker, the water in the jet is continuous with the water in the pool, and the air cavity is entrained at the moment of impact.

The cross-sectional shape of this air cavity is affected by the details of the wave behavior as it approaches breaking and, in short breaking waves, by surface tension. Calculations by Tulin (1996), Chen et al. (1999), and Song & Sirviente (2004) have shown that increasing the effect of surface tension (essentially decreasing the gravity wavelength) causes the plunging jet to thicken and reduces the volume of air entrapped at jet impact. When the effect of surface tension becomes dominant, the plunging jet is replaced by a bulge-capillary system as reported in the calculations and theory of Mui & Dommermuth (1995), Tulin (1996), Longuet-Higgins (1997), Longuet-Higgins & Dommermuth (1997), and Ceniceros & Hou (1999) and the experiments of Duncan et al. (1994, 1999). In these surface-tension-dominated waves, the transition to turbulence is initiated by flow separation at the leading edge (or toe) of the bulge (see Qiao & Duncan 2001), and air entrainment is reduced dramatically.

The shape of the cavity created at jet impact has been addressed theoretically using potential flow theory without surface tension by Longuet-Higgins (1982) and New (1983), whereas Greenhow (1983) has provided a theory predicting the shape of the entire crest region. Numerous numerical calculations have predicted the shape of the air cavity just before or at the moment of jet impact, and these include potential flow boundary-element calculations without surface tension by Longuet-Higgins & Cokelet (1976), Vinje & Brevig (1980, 1981), Dalrymple & Rogers (2006), and Grilli et al. (1997); potential flow boundary-element calculations with surface tension by Yao et al. (1994), Tulin (1996), and Longuet-Higgins & Dommermuth (1997); smooth particle hydrodynamics calculations by Dommermuth et al. (1988) and Landrini et al. (2007); direct numerical simulations of the Navier-Stokes equations by Chen et al. (1999), Song & Sirviente (2004), and Iafrati (2009), and large eddy simulations by Watanabe et al. (2005) and Lubin et al. (2006). A good example of the range of cavity shapes found when solitary waves of different heights approach a beach of the same slope can be found in Grilli et al. (1997, figure 3).

Experimental measurements of the shape of the entrapped air cavity are typically performed using photographs taken through the transparent sidewall of a wave tank. Such photographs and/or tracings of the wave and cavity profile are given in a number of articles, including Miller (1972), Bonmarin (1989), Perlin et al. (1996), and Blenkinsopp & Chaplin (2007, 2008). Longuet-Higgins predicted in his theory a cubic spline shape for this cavity and showed a favorable comparison of the theoretical cavity shape with a photograph from Miller (1972) (Longuet-Higgins 1982, figure 9). Blenkinsopp & Chaplin (2008) also compared their measurements with the cavity shape predicted by Longuet-Higgins (1982), and Bonmarin (1989) presented a comparison between his measurements and the cavity shape predicted by New (1983).

Few of the above-mentioned studies address air entrainment, so there are only a few that give measurements of the volume of air entrapped by jet impact. Exceptions are the experimental studies of Lamarre & Melville (1991) and Blenkinsopp & Chaplin (2007, 2008) and the numerical study of Iafrati (2009). These studies use very different wave-generation methods: Lamarre & Melville (1991) used a dispersive focusing method in water with intermediate, constant depth; Blenkinsopp & Chaplin (2007, 2008) used waves induced to break in deep water after propagating over a shoal; and Iafrati (2009) used a periodic wave train with an unstable initial wave shape to induce breaking. Blenkinsopp & Chaplin (2007, 2008) reported values of A_0/H_b^2 , where A_0 is the cross-sectional area of the entrapped air and H_b is the crest-to-trough wave height at incipient breaking, ranging from approximately 0.04 to 0.4, and the numerical calculations of Iafrati (2009) give values of 0.053 to 0.148. Lamarre & Melville (1991) examined three waves ranging from strong plunging to weak plunging/strong spilling and reported values of A_0 but not H_b . To find approximate values of A_0/H_b^2 , we estimated H_b by taking the average wave-packet frequency ($f_0 = 0.88$ Hz), using the dispersion relationship for waves in finite-depth water $f_0^2 = gk \tanh(kD)$ to obtain the wavelength, $\lambda_0 = 2\pi/k$, and choosing $H_b \approx 1/7\lambda_0$. The resulting values of A_0/H_b^2 from Lamarre & Melville's measurements ranged from 0.0291 to 0.114.

After initial impact, in all the breaking-wave experiments and calculations found for this article, the jet tip does not penetrate into the wave face. Rather, the behavior is as depicted in the smooth particle hydrodynamics calculations of Dalrymple & Rogers (2006) (see **Figure 13**) in which the

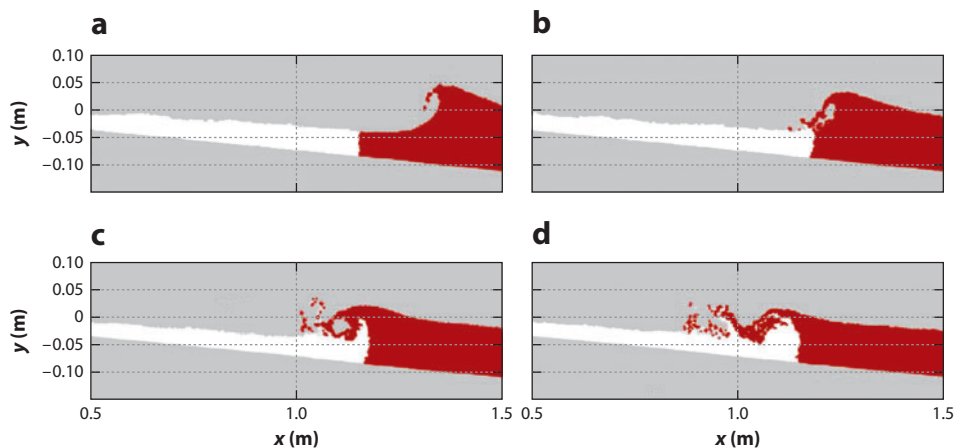


Figure 13

Two-dimensional smooth particle hydrodynamics calculations of a wave breaking on a sloped bottom. The entrapped volumes are empty (contain no air) and therefore can shrink to zero size. Some of the fluid particles are marked in red and show the fate of the fluid in the plunging jet after impact. Figure taken from Dalrymple & Rogers (2006).

particles in the jet are seen to form part of the forward splash and the inner surface of the cavity under the crest created by the initial jet impact. This behavior is of course markedly different than in that seen in all the studies mentioned in Section 2 in which the jet penetrates the pool, creating underwater craters of air.

To compare plunging jet impact behavior in breaking waves with the prototypical plunging jets discussed in Section 2, one must quantify the details of the breaking-wave jet tip speed and trajectory just prior to impact and the flow conditions at the impact site on the front face of the wave for typical breaking conditions. As depicted in **Figure 10a**, in the reference frame moving with the wave crest, the jet tip is moving at an angle relative to horizontal just before impact, and the water on the front face of the wave at the impact site is primarily flowing parallel to the surface, in the upslope direction (toward the wave crest). Once formed, the jet tip follows a nearly ballistic trajectory until it collides with the wave face. The constant horizontal jet speed in the reference frame of the crest, $(U_j)_x$, has been reported by a number of investigators—for example, van Dorn & Pazan (1975), Liu & Duncan (2003), and Shakeri et al. (2009) found $(U_j)_x = 0.08c$ to $0.15c$ (where c is the wave phase speed) in deep-water breaking-wave experiments; New et al. (1985) found $(U_j)_x = 0.32c$ to $1.59c$ in potential flow boundary-element calculations of breakers in shallow water; and Chen et al. (1999) found $(U_j)_x = 0.45c$ to $0.76c$ in viscous flow calculations of short-wavelength surface-tension-dominated breakers in deep water. Vertical accelerations of the jet tip ranging from $0.6g$ to $0.8g$ have been reported in the experiments of Liu & Duncan (2003) and Shakeri et al. (2009). That the vertical accelerations are less than g may be caused by temporal evolution in the jet tip shape due to surface tension (the wavelengths in the above-mentioned studies ranged from approximately 0.7 m to 2 m, and the jet thicknesses are probably less than 1 cm), the effect of air being squeezed out from inside the curl as the cavity closes (e.g., see Chen et al. 1999), or the fact that the jet tip is a geometrical point rather than the center of mass of an object in free fall.

The jet impact angle as determined in the reference frame of the wave crest, can be measured either from the centerline of the jet (as seen in a photograph of the breaker at the moment of jet impact) or from the angle of the jet tip velocity vector; because of the unsteadiness of the flow, these two angles need not be equal. For three breakers ranging from weakly to strongly plunging, Shakeri et al. (2009) found jet impact angles from 45° to 70° as measured from the jet centerline relative to horizontal and approximately 60° to 80° as measured from the jet tip velocity. Although the slope of the wave face at the impact site was not measured, estimates from the plots and images indicate that it was less than approximately 15° from horizontal.

The final quantity needed to compare a plunging breaker jet impact with a prototypical jet impact is the relative fluid velocity in the wave face. In the experiments of Shakeri et al. (2009), the flow speed on the wave face was not measured and, although certainly available in any of the numerical studies, was not typically reported other than through velocity vector field plots in the laboratory reference frame (e.g., see Chen et al. 1999, Lubin et al. 2006, Song & Sirvienta 2004). However, using the steady Bernoulli equation on the streamline that, in the reference frame moving with the crest, extends along the free surface from the impact point to the jet tip, one finds that the speed of the jet tip and the speed in the flow at the impact site are equal. This approximation should be relatively good as the ratio of the order of magnitude of the unsteady term to the flow speed squared term in Bernoulli's equation is

$$\frac{\partial\phi}{\partial t} / q^2 \sim \frac{cH}{T} / c^2 = \frac{H}{\lambda},$$

where H is the wave height above the mean water level, c is the phase speed, T is the wave period, and the linear dispersion relation for gravity waves has been used. Thus the $\partial\phi/\partial t$ term

is on the order of a factor of $H/\lambda \approx 0.1$ less than the flow speed squared term in Bernoulli's equation.

In examining the prototypical jet impact studies reviewed in Section 2, one finds that the one that most closely mimics the conditions of a plunging breaker is that of Gomez-Ledesma et al. (2011) in which a transient 2D plunging jet impact is examined as a jet nozzle translates over a quiescent liquid pool. In these experiments, the jet tip speed just before impact in the reference frame of the nozzle ranged from 2.12 to 3.48 m s⁻¹, the jet impact angle as measured from the jet tip trajectory in the reference frame of the jet nozzle varied from 92.9° to 44.8° relative to horizontal, the jet thickness ranged from 2.8 to 5 mm, and the translation speeds ranged from 0.0 to 0.6 m s⁻¹. The behavior here was markedly different than that in plunging breakers; in all cases, the jet penetrated the surface of the pool, creating large craters upstream and downstream of the jet that eventually pinched off at a depth below the mean water level, entrapping pockets of air in front of and behind the jet. There are many differences between the jet impact conditions in these experiments and those in a plunging breaker, but perhaps the largest difference is the ratio of the jet impact speed to the flow speed at the impact site, which is greater than 3.5 in all cases studied by Gomez-Ledesma et al. (2011) and, from the above order-of-magnitude analysis, is about equal to 1 in the plunging breaker. As mentioned in Section 2.4.3, Gomez-Ledesma et al. (2011) also found from theory that for a jet penetration solution to exist in their steady potential flow analysis, the jet translation speed must be less than the jet speed. Thus higher jet translation speeds in their experiments may have produced nonpenetrating jet impacts as in a plunging breaker.

The air entrainment that occurs after the initial jet impact is quite significant as found in the measurements of Lamarre & Melville (1991, 1994), Blenkinsopp & Chaplin (2007, 2008), and others. Blenkinsopp & Chaplin (2007) used optical probes to measure the void fraction distribution in three breakers in deep water, and **Figure 14** presents photographs and corresponding void

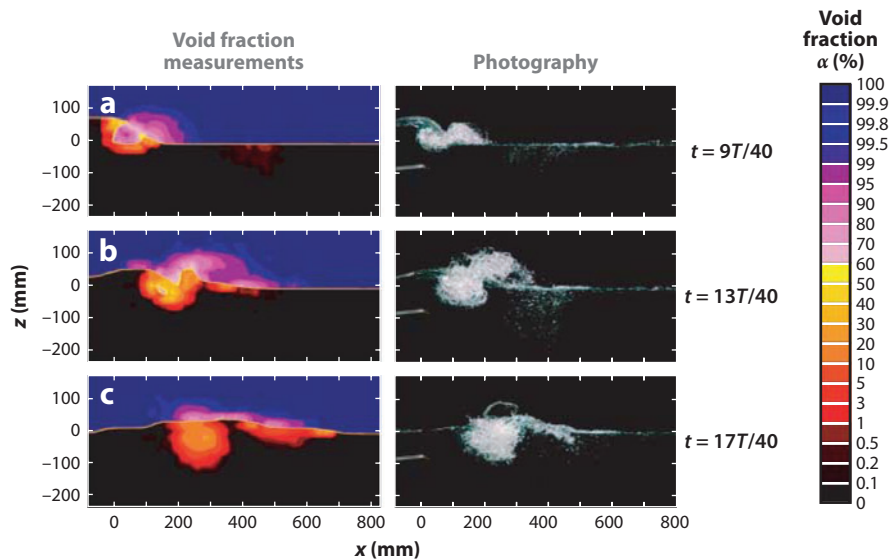


Figure 14

(Left column) Void fraction measurements and (right column) photographs of air entrained in a plunging breaker: (a) $t = 9T/40$, (b) $t = 13T/40$, and (c) $t = 17T/40$, where T is the wave period. Figure taken from Blenkinsopp & Chaplin (2007).

fraction maps from one of their waves. They found that the maximum air entrained per unit span reached approximately $1.6A_0$, where A_0 is the area of the cavity of air entrapped at the moment of jet impact. In this measurement, the area of entrained air is defined as the area of air between the 50% and 0.3% void fraction contours at any instant in time. The 50% boundary is of course arbitrary, and its relationship to the highest surface that can be drawn without leaving water is not known. They also found that the water volume per unit depth in the zone of void fractions between 50% and 99.7% reaches approximately $1.6A_0$.

Although the initial entrainment at the moment of jet impact is primarily a 2D event, as seen in the top-view image in **Figure 11a**, the subsequent flow is turbulent and highly 3D. An early indication of this three-dimensionality is the breakup of the tube of air under the crest. From **Figure 11b**, it can be seen that only 92 ms after the initial jet impact, the tube of air has broken down into a series of 3D bubbles. In a more violent version of the wave depicted in the photographs or a breaker with a larger wavelength, the air-tube breakup process creates a much wider distribution of bubble sizes. This breakup can of course be captured only in 3D calculations, and owing to resolution issues, the full bubble size distribution cannot be computed at this time.

There are several post-jet impact entrainment mechanisms, all involving the splash generated by the main plunging jet impact. The first mechanism is entrainment by the impact of the disorganized jet created at the front of the splash. Some investigators have reported several cycles of splash and impact, with each subsequent impact entrapping a smaller amount of air. The first splash impact is seen clearly in the calculations illustrated in **Figures 13c** and **15b**. Similar effects are found in other calculations (e.g., see Chen et al. 1999, Iafrati 2009, Watanabe et al. 2005). The first splash impact is about to occur in the side-view and top-view photographs in **Figure 11b,f**, respectively. In this weak, small-scale plunger, the top view shows only a few bubbles in the splash zone at this time. **Figure 12** shows a short sequence of close-up images from the same top-view movie used to produce **Figures 11a–d** (see **Supplemental Video 9**). The photographs were taken at 4-ms intervals and show the entrainment of a single bubble during the subsequent splash impact process. The sequence shows that even at this small scale at which surface tension appears to be playing a strong role, the entrainment process is highly 3D.

The second entrainment mechanism occurs between the side of the splash closest to the jet and the top surface of the jet (see **Figure 10c**). Numerical calculations frequently show a large volume of air entrapped suddenly as the splash seems to move backward relative to the smooth upper surface of the jet. An example of this entrainment from the calculations of Landrini et al. (2007) is shown in **Figure 15c** and can be found in numerous other studies (e.g., see Iafrati 2009, Watanabe et al. 2005). Entrainment in this location is also frequently mentioned in experimental studies and is perhaps best visualized from underwater photographs (e.g., see Blenkinsopp & Chaplin 2007, 2008; Bonmarin 1989; Miller 1972). As can be seen from the top-view and above-surface side-view images in **Figure 11**, it is not hard to imagine this type of entrainment occurring, but it is not clearly visible. From the experiments, it is also unclear if the entrainment occurs only suddenly or via a continuous entrainment of air at the minimum in the profile at which the splash meets the jet.

The last mechanism is entrainment all over the splash zone due to the very strong turbulence in this region and due to the advancing front in the later stages of the breaking process, when the front region of the splash is similar to the front of a strong spilling breaker. The entrainment over the surface of the splash zone is created by subsurface turbulent eddies interacting with the free surface and is of course highly 3D. The entrainment at the front of the splash zone appears also to be driven by the turbulent eddies but is probably aided by the downslope nature of the front

 **Supplemental Material**

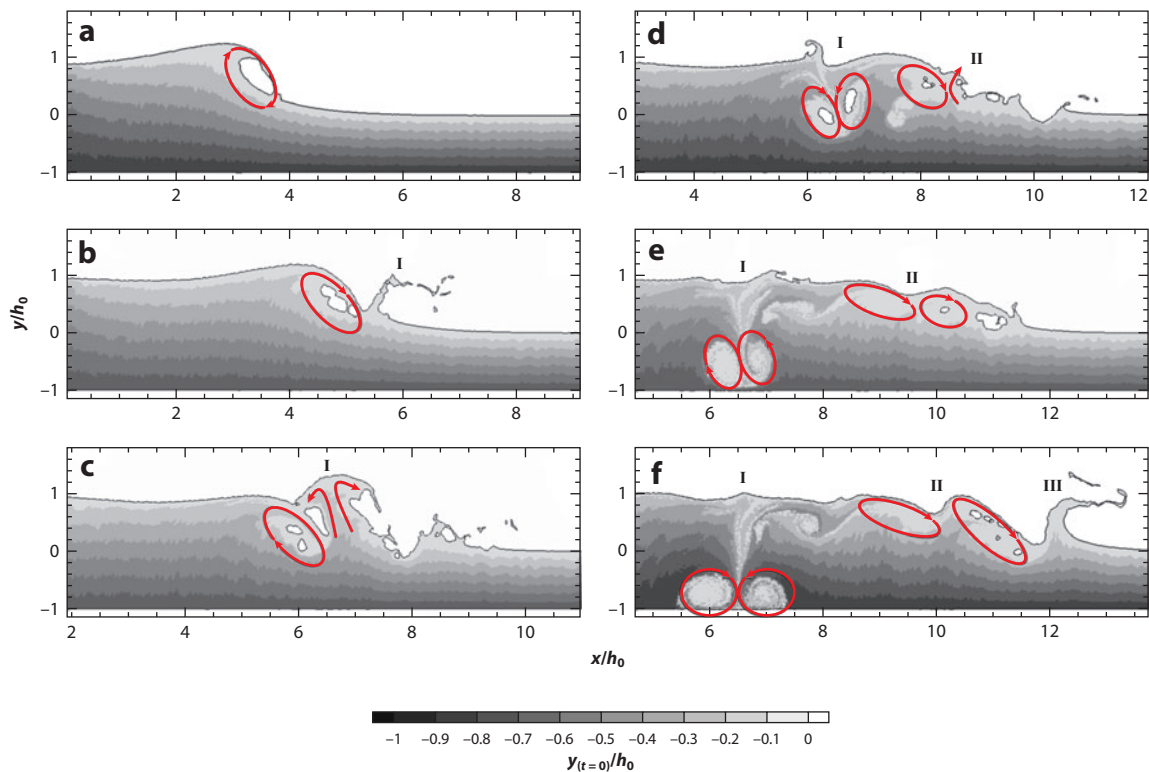


Figure 15

Two-dimensional smooth particle hydrodynamics calculations of a plunging breaker generated by a vertical wall at the left, moving horizontally to the right. The entrapped volumes are empty (contain no air) and therefore can shrink to zero size. The closed red contours show the sign of the circulation around each cavity, and the arrows indicate flow direction. The roman numerals I, II and III refer to the sequence of splash-ups from the impact of the plunging jet, the impact of splash-up I and the impact of splash-up II, respectively. Figure taken from Landrini et al. (2007).

motion. The photographs of this front, as seen in the side- and top-view images of **Figure 11d,b**, clearly show the 3D character of this front. The effect of scale is extremely important here, as can be seen by comparing the relatively smooth surface of the splash in the meter-long breaker in **Figure 11** to the photograph of a larger breaker on a beach as in **Figure 16** in which there are probably so many droplets and ligaments of water that the surface of the splash is not clearly defined. As noted by Brocchini & Peregrine (2001a,b), entrainment occurs in this type of flow when both the turbulent Weber number, $We = \rho Lu^2/\sigma$, and the turbulent Froude number, $Fr = u'^2/gL$, exceed critical values, where u' and L are the velocity and length scales of the turbulence, respectively. Both dimensionless ratios increase with increasing u' , and to first order, u' will increase with the wave-phase speed, which for deep-water waves increases as the square root of the wavelength. Also, for a given breaker wavelength, u' will increase as the plunging becomes more violent, which occurs when the horizontal velocity component of the jet is larger. As this velocity component increases, the distance of the impact point from the crest increases, as does the vertical velocity component at impact as the jet falls farther before impact. In a strong plunging breaker, in which the jet impact site is close to the mean water level, these speeds would be of the order of the wave-phase speed.



Figure 16

A plunging breaker approaching a beach at Big Sur, California, 2009.

4. CONCLUSIONS

Air entrainment into liquids occurs across a wide parametric space, and as a result, a diverse set of mechanisms is exhibited to overcome the stabilizing forces of surface tension and gravity. The bulk of the work in previous years examined steady jet flows. For viscous liquids that are dominated by steady shear stresses at the jet/pool interface, this has produced useful results, as shown by the recent success in using the ideas of a viscous fracture and a critical capillary scaling to predict the entrainment threshold and entrainment rate. For entrainment by low-viscosity liquids, however, a simple steady analysis is complicated by a profound sensitivity to fluctuating disturbances on the incoming flow and the receiving-pool conditions. Additionally, the practical expediency of correlating the air entrainment with the upstream jet conditions has produced a plethora of empirical correlations, but the synthesis of these correlations into a comprehensive air-entrainment model remains elusive.

One possible means forward is to adopt a perspective characterizing the dynamics of the transient conditions at the jet/pool interface. Only recently have transient impacts been studied, both as a fundamental class of problems (e.g., a starting jet) and as a model to understand how disturbances play a role in the entrainment process. This work has provided a connection between entrainment by droplet impacts and that due to small bump disturbances on laminar nonentraining jets, indicating a common dependence in the volume of air entrained on the jet/drop Froude number and the size of the disturbance. What is still missing and should be a focus of future work concerns the details of how this process is related to other mechanisms, such as subsurface vorticity, as well as a dependence on surface tension and viscosity.

When one further examines the application of air entrainment in plunging breaking waves, making a connection to the prototypical plunging jet becomes even more difficult. The plunging jet in a breaking wave is a transient self-generated feature that occurs in a range of impact angles and translation velocities that have not been explored in isolated jet studies. Wave-plunging jet conditions appear to produce a qualitatively different type of impact, with almost no penetration

into the oncoming flow and a pronounced splash that cascades multiple times down the face of the wave. What is well characterized to date is the volume of air trapped by the initial contact of the jet with the wave face, which has been predicted by numerical simulations, and its shape is predicted by theory for a limited set of conditions. In need of further attention are all the subsequent processes that follow the initial contact, as these are only known qualitatively for the majority of the breaking conditions.

As a final closing comment to this discussion, we acknowledge that a mechanistic approach from direct observation also has its limitations, particularly when there is the potential for the nonlinear interactions of multiple dynamic processes. As a case in point, it is sobering to compare the images of the field-scale plunging breaking wave shown in **Figure 16** with the smaller-scale laboratory conditions shown in **Figures 11** and **12**. In the latter, the flow is clearly complicated and stochastic, but regions of specific behavior can be identified and likely modeled. In the field-scale conditions, many of these processes overlap, and the wide range of scales present produces an intense multiphase foam/spray/bubbly mixture within which it is difficult to discern what is happening mechanistically. When constructing appropriate mechanisms, one then must rely primarily on the examination of derived quantities from quantitative measurement and simulation (phase-averaged velocity, concentration, phase-momentum coupling and interaction terms), which adds a further layer of complexity. Advances in instrumentation and simulation capabilities, however, do give hope for progress in this area as well.

FUTURE ISSUES

Concerning transient disturbances in prototypical plunging jets:

1. What is the role played by the submerged jet vorticity in destabilizing the interface?
2. What is the mechanism by which kinetic energy of the jet is made available to entrain air?
3. How does surface tension influence the entrained volume generated by bump disturbances?
4. How does asymmetry in the disturbance influence the shape and size of the entrained bubble?

Concerning air entrainment in plunging breaking waves:

5. How is the splash formed by the initial impact, and how much does it vary with wave conditions?
6. What role does the splash play in subsequent entrainment events, both via impacts further down the wave face and between the top of the plunging jet and the back of the splash?
7. What is the entrainment due to subsurface turbulence within the bulk and at the leading edge of the breaking zone?

DISCLOSURE STATEMENT

The authors are not aware of any biases that might be perceived as affecting the objectivity of this review.

ACKNOWLEDGMENTS

The authors would like to acknowledge the dedicated efforts of Mr. Jin Kevin Kim and Mr. Kyle Corfinan in their assistance in conducting the experiments that produced **Figures 5** and **6**, as well as Mr. Ren Liu who produced the images for **Figures 11** and **12**. The authors are also grateful for insightful discussions with Prof. Andrea Prosperetti over the years on this topic.

LITERATURE CITED

- Bick AG, Ristenpart WD, van Nierop EA, Stone HA. 2010. Bubble formation via multidrop impacts. *Phys. Fluids* 22:042105**
- Bin AK. 1988. Minimum air entrainment velocity of vertical plunging liquid jets. *Chem. Eng. Sci.* 43:379–89
- Bin AK. 1993. Gas entrainment by plunging liquid jets. *Chem. Eng. Sci.* 48:3585–630**
- Blenkinsopp CE, Chaplin JR. 2007. Void fraction measurements in breaking waves. *Proc. R. Soc. A* 463:3151–70
- Blenkinsopp CE, Chaplin JR. 2008. The effect of relative crest submergence on wave breaking over submerged slopes. *Coast. Eng.* 55:967–74
- Bonetto F, Drew D, Lahey RT. 1994. The analysis of a plunging liquid jet: the air entrainment process. *Chem. Eng. Commun.* 130:11–29
- Bonetto F, Lahey RT. 1993. An experimental study on air carryunder due to a plunging liquid jet. *Int. J. Multiphase Flow* 19:281–94
- Bonmarin P. 1989. Geometric properties of deep-water breaking waves. *J. Fluid Mech.* 209:405–33
- Brattberg T, Chanson H. 1998. Air entrainment and air bubble dispersion at two-dimensional plunging water jets. *Chem. Eng. Sci.* 53:4113–27
- Brocchini M, Peregrine DH. 2001a. The dynamics of strong turbulence at free surfaces. Part 1: Description. *J. Fluid Mech.* 449:225–54**
- Brocchini M, Peregrine DH. 2001b. The dynamics of strong turbulence at free surfaces. Part 2: Free-surface boundary conditions. *J. Fluid Mech.* 449:255–90
- Burgess JM, Molloy NA. 1973. Gas absorption in the plunging liquid jet reactor. *Chem. Eng. Sci.* 28:183–90
- Carroll K, Mesler R. 1981. Bubble nucleation studies. 2. Bubble entrainment by drop-formed vortex rings. *AIChE J.* 27:853–56
- Ceniceros HD, Hou TY. 1999. Dynamic generation of capillary waves. *Phys. Fluids* 11:1042–50
- Chanson H. 1996. *Air Bubble Entrainment in Free-Surface Turbulent Shear Flows*. New York: Academic
- Chanson H. 1997. Measuring air-water interface area in supercritical open channel flow. *Water Res.* 31:1414–20
- Chanson H. 2009. Turbulent air-water flows in hydraulic structures: dynamic similarity and scale effects. *Environ. Fluid Mech.* 9:125–42
- Chanson H, Manasseh R. 2003. Air entrainment processes in a circular plunging jet: void-fraction and acoustic measurements. *J. Fluids Eng.* 125:910–21
- Chen G, Kharif C, Zaleski S, Li J. 1999. Two-dimensional Navier-Stokes simulation of breaking waves. *Phys. Fluids* 11:121–33
- Chirichella D, Ledesma R, Kiger K, Duncan J. 2002. Incipient air entrainment in a translating axisymmetric plunging laminar jet. *Phys. Fluids* 14:781–90
- Ciborowski J, Bin A. 1972. Minimum entrainment velocity for free liquid jets. *Inz. Chem.* 2:557–77 (In Polish)
- Cummings P, Chanson H. 1997. Air entrainment in the developing flow region of plunging jets. Part 1: theoretical developments. *J. Fluids Eng.* 119:597–602
- Cummings P, Chanson H. 1999. An experimental study of individual air bubble entrainment at a planar plunging jet. *Chem. Eng. Res. Des.* 77:159–64
- Dalrymple R, Rogers B. 2006. Numerical modeling of water waves with the SPH method. *Coast. Eng.* 53:141–47
- Dommermuth DG, Yue DKP, Lin WM, Rapp RJ, Chan ES, Melville WK. 1988. Deep-water plunging breakers: a comparison between potential theory and experiments. *J. Fluid Mech.* 189:423–42

Demonstrates the reduced threshold required for air entrainment under multi-drop-impact conditions and suggested the importance of the free-surface motion prior to secondary impact as a key factor in controlling the entrainment.

Presents a comprehensive review through date of publication, covering jet breakup lengths, entrainment limit correlations, volume entrainment rates, bubble dispersion, and gas/liquid mass transfer.

Provides an excellent discussion of the physical processes controlling the motion of the free surface due to subsurface turbulent flow.

Summarizes the connection between the formation of a singular cusp and its eventual breakdown through viscous pumping within the gap that leads to air entrainment in viscous jets.

Presents a detailed study of wave breaking and air entrainment using 2D direct numerical simulations.

- Duclaux V, Caille F, Duez C, Ybert C, Bocquet L, Clanet C. 2007. Dynamics of transient cavities. *J. Fluid Mech.* 591:1–19
- Duncan JH, Philomin V, Behres M, Kimmel J. 1994. The formation of spilling breaking water waves. *Phys. Fluids* 6:2558–60
- Duncan JH, Qiao H, Philomin V, Wenz A. 1999. Gentle spilling breakers: crest profile evolution. *J. Fluid Mech.* 379:191–222
- Eggers J. 2001. Air entrainment through free-surface cusps. *Phys. Rev. Lett.* 86:4290–93**
- El Hammoumi M. 1994. *Entrainement d'air par jet plongeant vertical: application aux becs de remplissage pour le dosage ponderal*. PhD thesis. INPG, Grenoble, France
- El Hammoumi M, Achard JL, Davoust L. 2002. Measurements of air entrainment by vertical plunging liquid jets. *Exp. Fluids* 32:624–38
- Ervine DA, McKeough E, Elsaywy EM. 1980. Effect of turbulence intensity on the rate of air entrainment by plunging water jets. *Proc. Inst. Civ. Eng.* 69(Part 2):425–45
- Evans GM, Jameson GJ, Rielly CD. 1996. Free jet expansion and gas entrainment characteristics of a plunging liquid jet. *Exp. Therm. Fluid Sci.* 12:142–49
- Franz GJ. 1959. Splashes as sources of sound in liquids. *J. Acoust. Soc. Am.* 31:1080–96
- Galimov AY, Sahni O, Lahey RT, Shephard MS, Drew DA, Jansen KE. 2010. Parallel adaptive simulation of a plunging liquid jet. *Acta Math. Sci.* 30:522–38
- Gomez-Ledesma R, Kiger KT, Duncan JH. 2011. The impact of a translating plunging jet on a pool of the same liquid. *J. Fluid Mech.* 680:5–30
- Greenhow M. 1983. Free-surface flows related to breaking waves. *J. Fluid Mech.* 134:259–75
- Grilli ST, Svendsen IA, Subramanya R. 1997. Breaking criterion and characteristics for solitary waves on slopes. *J. Waterw. Port Coast. Ocean Eng.* 123:102–12
- Ho CM, Huerre P. 1984. Perturbed free shear layers. *Annu. Rev. Fluid Mech.* 16:365–424
- Iafrazi A. 2009. Numerical study of the effects of the breaking intensity on wave breaking flows. *J. Fluid Mech.* 622:371–411**
- Jeong JT, Moffatt HK. 1992. Free-surface cusps associated with flow at low Reynolds number. *J. Fluid Mech.* 241:1–22
- Joseph DD, Nelson J, Renardy M, Renardy Y. 1991. Two-dimensional cusped interfaces. *J. Fluid Mech.* 223:383–409
- Kersten B, Ohl CD, Prosperetti A. 2003. Transient impact of a liquid column on a miscible liquid surface. *Phys. Fluids* 15:821–24
- Kolaini A, Roy RA, Crum LA. 1991. An investigation of the acoustic emissions from a bubble plume. *J. Acoust. Soc. Am.* 89:2452–55
- Kolaini A, Roy RA, Crum LA, Yi M. 1993. Low-frequency underwater sound generation by impacting transient cylindrical water jets. *J. Acoust. Soc. Am.* 94:2809–20
- Korobkin AA, Pukhnachov VV. 1988. Initial stage of water impact. *Annu. Rev. Fluid Mech.* 20:159–85
- Kumagai M, Endoh K. 1983. A note on the relationship between gas entrainment curve and its starting velocity. *J. Chem. Eng. Jpn.* 16:74–75
- Lamarre E, Melville WK. 1991. Air entrainment and dissipation in breaking waves. *Nature* 351:469–72
- Lamarre E, Melville WK. 1994. Void-fraction measurements and sound-speed fields in bubble plumes generated by breaking waves. *J. Acoust. Soc. Am.* 95:1317–28
- Landau LD, Levich VG. 1942. Dragging of a liquid film by a moving plate. *Acta Physicochim. USSR* 17:42–54
- Landrini M, Colagrossi A, Greco M, Tulin MP. 2007. Gridless simulations of splashing processes and near-shore bore propagation. *J. Fluid Mech.* 591:183–213
- Lasheras JC, Hopfinger EJ. 2000. Liquid jet instability and atomization in a coaxial gas stream. *Annu. Rev. Fluid Mech.* 32:275–308
- Lezzi AM, Prosperetti A. 1991. The stability of an air film in a liquid flow. *J. Fluid Mech.* 226:319–47
- Lin JT, Donnelly HG. 1966. Gas bubble entrainment by plunging laminar liquid jets. *AICbE J.* 12:563–71
- Lin SP, Reitz RD. 1998. Drop and spray formation from a liquid jet. *Annu. Rev. Fluid Mech.* 30:85–105
- Liu X, Duncan JH. 2003. The effects of surfactants on spilling breaking waves. *Nature* 421:520–23
- Longuet-Higgins MS. 1982. Parametric solutions for breaking waves. *J. Fluid Mech.* 121:403–24

- Longuet-Higgins MS. 1997. Progress towards understanding how waves break. *Proc. 21st Symp. Nav. Hydrodyn.*, pp. 7–28. Washington, DC: Natl. Acad.
- Longuet-Higgins MS, Cokelet ED. 1976. Deformation of steep surface waves on water. 1. Numerical method of computation. *Proc. R. Soc. Lond. A* 350:1–26
- Longuet-Higgins MS, Dommermuth DG. 1997. Crest instabilities of gravity waves. 3. Nonlinear development and breaking. *J. Fluid Mech.* 336:33–50
- Lorenceau E. 2003. *Interfaces en grande deformation: oscillations, impacts, singularites*. PhD thesis. Univ. Paris VI
- Lorenceau E, Quéré D, Eggers J. 2004. Air entrainment by a viscous jet plunging into a bath. *Phys. Rev. Lett.* 93:254501
- Lorenceau E, Restagno F, Quéré D. 2003. Fracture of a viscous liquid. *Phys. Rev. Lett.* 90:184501
- Lubin P, Vincent S, Abadie S, Caltagirone JP. 2006. Three-dimensional large eddy simulation of air entrainment under plunging breaking waves. *Coast. Eng.* 53:631–55
- Ma J, Oberai AA, Drew DA, Lahey RT, Moraga FJ. 2009. A quantitative sub-grid air entrainment model for bubbly flows: plunging jets. *Comput. Fluids* 39:77–86
- May A. 1952. Vertical entry of missiles into water. *J. Appl. Phys.* 23:1362–72
- McKeogh E. 1978. *A study of air entrainment using plunging water jets*. PhD thesis. Queen's Univ. Belfast
- McKeogh EJ, Ervine DA. 1981. Air entrainment rate and diffusion pattern of plunging liquid jets. *Chem. Eng. Sci.* 36:1161–72
- Miller RL. 1972. Study of air entrainment in breaking waves. *Am. Geophys. Union Trans.* 53:426
- Mui RCY, Dommermuth DG. 1995. The vortical structure of parasitic capillary waves. *J. Fluids Eng.* 117:355–61
- New AL. 1983. A class of elliptical free-surface flows. *J. Fluid Mech.* 130:219–39
- New AL, McIver P, Peregrine DH. 1985. Computations of overturning waves. *J. Fluid Mech.* 150:233–51
- Oguz HN. 1998. The role of surface disturbances in the entrainment of bubbles by a liquid jet. *J. Fluid Mech.* 372:189–212
- Oguz HN, Prosperetti A. 1990. Bubble entrainment by the impact of drops on liquid surfaces. *J. Fluid Mech.* 219:143–79
- Oguz HN, Prosperetti A, Kolaini A. 1995. Air entrainment by a falling water mass. *J. Fluid Mech.* 294:181–207**
- Oguz HN, Prosperetti A, Lezzi AM. 1992. Examples of air-entraining flows. *Phys. Fluids A* 4:649–51
- Ohl CD, Oguz HN, Prosperetti A. 2000. Mechanism of air entrainment by a disturbed liquid jet. *Phys. Fluids* 12:1710–14
- Perlin M, He J, Bernal LP. 1996. An experimental study of deep water plunging breakers. *Phys. Fluids* 8:2365–74
- Prosperetti A, Crum LA, Pumphrey HC. 1989. The underwater noise of rain. *J. Geophys. Res.* 94:3255–59
- Pumphrey HC, Crum LA, Bjorno L. 1989. Underwater sound produced by individual drop impacts and rainfall. *J. Acoust. Soc. Am.* 85:1518–26
- Pumphrey HC, Elmore PA. 1990. The entrainment of bubbles by drop impacts. *J. Fluid Mech.* 220:539–67
- Qiao H, Duncan JH. 2001. Gentle spilling breakers: crest flow-field evolution. *J. Fluid Mech.* 439:57–85
- Rein M. 1993. Phenomena of liquid-drop impact on solid and liquid surfaces. *Fluid Dyn. Res.* 12:61–93
- Rodriguez F, Mesler R. 1988. The penetration of drop-formed vortex rings into pools of liquid. *J. Colloid Interface Sci.* 121:121–29
- Sene KJ. 1988. Air entrainment by plunging jets. *Chem. Eng. Sci.* 43:2615–23
- Shakeri M, Tavakolinejad M, Duncan JH. 2009. An experimental investigation of divergent bow waves simulated by a two-dimensional plus temporal wave maker technique. *J. Fluid Mech.* 634:217–43; Erratum. 638:507
- Soh WJ, Khoo BC, Yuen WYD. 2005. The entrainment of air by water jet impinging on a free surface. *Exp. Fluids* 39:496–504
- Song CY, Sirviente AL. 2004. A numerical study of breaking waves. *Phys. Fluids* 16:2649–67
- Tulin MP. 1996. Breaking of ocean waves and downshifting. In *Waves and Nonlinear Processes in Hydrodynamics*, ed. JE Grue, B Gjevik, J Weber, pp. 177–90. Dordrecht: Kluwer Acad.
- van de Sande E. 1974. *Air entrainment by plunging water jets*. PhD thesis, Tech. Hogesch. Delft
- van de Sande E, Smith JM. 1973. Surface entrainment of air by high-velocity water jets. *Chem. Eng. Sci.* 28:1161–68

Develops Froude-scaling arguments for cavity collapse and air entrainment by the transient impact of a liquid mass, providing a basis for much of the subsequent work.

Discusses the flow structures and air entrainment in spilling and plunging breaking waves using 3D large-eddy simulations.

Demonstrates the role of isolated jet surface disturbances in entraining air in otherwise nonentraining conditions.

- van de Sande E, Smith JM. 1976. Jet break-up and air entrainment by low velocity turbulent water jets. *Chem. Eng. Sci.* 31:219–24
- van Dorn WG, Pazan SE. 1975. Laboratory investigation of wave breaking. Part II: deep water waves. *Tech. Rep. 75-21*, Scripps Inst. Ocean., San Diego
- Villermaux E. 2007. Fragmentation. *Annu. Rev. Fluid Mech.* 39:419–46
- Vinje T, Brevig P. 1980. Breaking waves on finite water depths: a numerical study. *Ship Res.* 6:497–503
- Vinje T, Brevig P. 1981. Numerical simulation of breaking waves. *Adv. Water Resour.* 4:77–82
- Watanabe Y, Saeki H, Hosking RJ. 2005. Three-dimensional vortex structures under breaking waves. *J. Fluid Mech.* 545:291–328**
- Winant CD, Browand FK. 1974. Vortex pairing: mechanism of turbulent mixing layer growth at moderate Reynolds number. *J. Fluid Mech.* 63:237–55
- Wood I. 1991. *Hydraulic Design Considerations*. IAHR Hydraul. Struct. Des. Man. 4. Rotterdam: Balema
- Yao Y, Wang P, Tulin M. 1994. Wave groups, wave-wake interactions and wave breaking: results of numerical simulations. *Proc. 20th Symp. Nav. Hydrodyn.*, pp. 551–67. Washington, DC: Natl. Acad.
- Zhu Y, Oguz H, Prosperetti A. 2000. On the mechanism of air entrainment by liquid jets at a free surface. *J. Fluid Mech.* 404:151–77**



Contents

Aeroacoustics of Musical Instruments <i>Benoit Fabre, Joël Gilbert, Avraham Hirschberg, and Xavier Pelorson</i>	1
Cascades in Wall-Bounded Turbulence <i>Javier Jiménez</i>	27
Large-Eddy-Simulation Tools for Multiphase Flows <i>Rodney O. Fox</i>	47
Hydrodynamic Techniques to Enhance Membrane Filtration <i>Michel Y. Jaffrin</i>	77
Wake-Induced Oscillatory Paths of Bodies Freely Rising or Falling in Fluids <i>Patricia Ern, Frédéric Risso, David Fabre, and Jacques Magnaudet</i>	97
Flow and Transport in Regions with Aquatic Vegetation <i>Heidi M. Nepf</i>	123
Electrorheological Fluids: Mechanisms, Dynamics, and Microfluidics Applications <i>Ping Sheng and Weijia Wen</i>	143
The Gyrokinetic Description of Microturbulence in Magnetized Plasmas <i>John A. Krommes</i>	175
The Significance of Simple Invariant Solutions in Turbulent Flows <i>Genta Kawahara, Markus Uhlmann, and Lennaert van Veen</i>	203
Modern Challenges Facing Turbomachinery Aeroacoustics <i>Nigel Peake and Anthony B. Parry</i>	227
Liquid Rope Coiling <i>Neil M. Ribe, Mehdi Habibi, and Daniel Bonn</i>	249
Dynamics of the Tear Film <i>Richard J. Braun</i>	267
Physics and Computation of Aero-Optics <i>Meng Wang, Ali Mani, and Stanislav Gordeyev</i>	299

Smoothed Particle Hydrodynamics and Its Diverse Applications <i>J. J. Monaghan</i>	323
Fluid Mechanics of the Eye <i>Jennifer H. Siggers and C. Ross Ethier</i>	347
Fluid Mechanics of Planktonic Microorganisms <i>Jeffrey S. Guasto, Roberto Rusconi, and Roman Stocker</i>	373
Nanoscale Electrokinetics and Microvortices: How Microhydrodynamics Affects Nanofluidic Ion Flux <i>Hsueh-Chia Chang, Gilad Yossifon, and Evgeny A. Demekhin</i>	401
Two-Dimensional Turbulence <i>Guido Boffetta and Robert E. Ecke</i>	427
“Vegetable Dynamicks”: The Role of Water in Plant Movements <i>Jacques Dumais and Yoël Forterre</i>	453
The Wind in the Willows: Flows in Forest Canopies in Complex Terrain <i>Stephen E. Belcher, Ian N. Harman, and John J. Finnigan</i>	479
Multidisciplinary Optimization with Applications to Sonic-Boom Minimization <i>Juan J. Alonso and Michael R. Colonno</i>	505
Direct Numerical Simulation on the Receptivity, Instability, and Transition of Hypersonic Boundary Layers <i>Xiaolin Zhong and Xiaowen Wang</i>	527
Air-Entrainment Mechanisms in Plunging Jets and Breaking Waves <i>Kenneth T. Kiger and James H. Duncan</i>	563
Indexes	
Cumulative Index of Contributing Authors, Volumes 1–44	597
Cumulative Index of Chapter Titles, Volumes 1–44	606

Errata

An online log of corrections to *Annual Review of Fluid Mechanics* articles may be found at <http://fluid.annualreviews.org/errata.shtml>